Dynamics of Electronic Transfer Processes at Metal/Insulator Interfaces

J. Güdde, W. Berthold, and U. Höfer*

Fachbereich Physik und Zentrum für Materialwissenschaften, Philipps-Universität, D-35032 Marburg, Germany

Received December 20, 2005

Contents

1. Introduction

The coupling of electronic excitations at surfaces to the bulk material is the key to a variety of dynamical processes. It governs very diverse phenomena such as charge transfer across interfaces in small scale electronic devices,[1,2] desorption and dissociation processes of adsorbates induced by electronic excitations,[3,4,5] nonadiabatic effects observed for adsorption of molecules at surfaces,[6] and even chemical reactions at surfaces in general. In the past few years, enormous progress, both in the experimental and theoretical methods, has been achieved to precisely measure and predict the lifetimes of occupied and unoccupied electronic states at pure metal surfaces.[7] The advancement was particularly remarkable in the case of image-potential states which represent a prototype of electronic states at a metal surface. The well-known properties of these hydrogen-like states makes them an ideal probe of the electronic decay at surfaces due to the many-body interactions between surface and bulk electrons. Time-resolved two-photon photoemission (2PPE) experiments and accurate many-body calculations have led to a good understanding of many aspects of the electronic decay of these hydrogen-like states at metal surfaces.[7−24]

In addition to internal electronic excitations, adsorbates may introduce new electronic states at a surface, which are derived from the electronic states of the free atom or molecule and which are involved in the chemical bonding of the adsorbate to the surface. The understanding of charge transfer between metal and adsorbate will rely on detailed knowledge of the coupling of such states to the metal surface. This is in general a very complex task which will be further complicated by the fact that the image-potential will always be superimposed and lead to a modification of the electronic structure of the adsorbate/metal complex. For adsorbates that do not introduce unoccupied electronic levels around the vacuum energy, however, the image-potential states will retain their simple character. In this case, the influence of the adsorbate on the electronic structure at the surface can be described as a modification of the image-potential states. Such adsorbate layers can modify the coupling of image-potential states to the metal substrate very strongly and cause a drastic change of their inelastic lifetimes due to a repelling of the image-potential states from the surface.[25,26,27] In addition, some molecular adsorbates were shown to give rise to two-dimensional localization of these states.[28,29,30]

For a detailed understanding of the effect of decoupling of image-potential states by adsorbate layers, the study of rare-gas layers is most promising because of their layer-by-layer growth and their well-characterized electronic structure. As will be discussed below, the energetic position of the bulk conduction band, derived from the unoccupied 6s (5s, 4s) level of the Xe (Kr, Ar) atoms, is the crucial factor that determines the layer-dependent dynamics of image-potential states. If the electron affinity is negative, as in the case of Ar, the insulator film represents a repulsive barrier and the image-potential states are strongly decoupled from the metal surface. Here, the image-potential states persist on the surface of the adlayer even in the limit of macroscopic thicknesses. For a positive electron affinity, as is the case for Xe and Kr, the layer potential is slightly attractive and can give rise to quantum-well states in the layer.

For thick adsorbate films, the image-potential of the metal which is screened within the adlayer leads to the formation of new electronic states with similar properties to those of image-potential states at the surface, but spatially located at the interface. The existence of these interface states has been recently demonstrated for Ar/Cu(100).[31] Their decay dynamics could be studied by time- and momentum-resolved 2PPE even for layer thicknesses of up to 200 Å, which is much larger than the spatial extent of the wave function. This study

* To whom correspondence should be addressed. E-mail: Hoefer@physik.uni-marburg.de.

10.1021/cr050171s CCC: $59.00
Published on Web 09/22/2006

Jens Güdde was born in Berlin and obtained his diploma in 1991 and his Ph.D. degree in 1995 from the Free University of Berlin, for work on high-resolution laser spectroscopy of Rydberg atoms. After his Ph.D., he started to work on ultrafast laser spectroscopy and joined the Max-Born-Institute for Nonlinear Optics and Short Pulse Spectroscopy in Berlin from 1996 to 1997, where he investigated the ultrafast dynamics of ammonia clusters using femtosecond VUV laser pulses. In 1997, he returned to the Free University of Berlin and worked as project leader on nonlinear optics and ultrafast spin dynamics in thin metallic films. He joined the group of Prof. Dr. Höfer at the Philipps University in Marburg in 2000, where he studies the ultrafast electron dynamics at metal surfaces using two-photon photoemission and nonlinear optical spectroscopy. For this work, he received his habilitation for experimental physics in 2006.

Wolfram Berthold obtained his diploma in physics in 1995 from the Technical University of Munich, Germany. As part of his Ph.D. work under the direction of Prof. Höfer at the Max-Planck-Institute for Quantum Optics in Garching (1996–2000), he set up a time-resolved two-photon photoemission experiment for surface studies and investigated ultrafast electron-transfer processes at rare-gas/metal interfaces. From 2001 to 2004, he worked as a senior researcher in the group of Prof. Höfer at the University of Marburg. In 2005, he joined Infineon/Qimoda AG in Dresden, Germany.

Ulrich Höfer received a Ph.D. degree in physics in 1989 from the Technical University of Munich, Germany, for work on photoelectron spectroscopy of adsorbates at surfaces. After spending two years as a visiting scientist at the IBM Thomas J. Watson Research Center in Yorktown Heights, New York, he joined the Max-Planck-Institute for Quantum Optics in Garching, Germany. In 1999 he became a full professor for experimental physics at the Philipps University in Marburg. His main research interests are laser spectroscopy of surfaces and interfaces, coherence phenomena and ultrafast processes at surfaces, as well as the dynamics of elementary adsorbate reactions. He was awarded the Arnold-Sommerfeld Prize of the Bavarian Academy of Sciences in 1995 for his work on hydrogen adsorption on silicon.

became feasible by promoting the electrons from the interface states into the Ar conduction band. There, the electrons undergo ballistic transport without noticeable inelastic or elastic losses to the Ar surface, where they can emerge into the vacuum. This shows that in favorable cases 2PPE can be used to investigate the electron dynamics not only for thin film systems but also at buried interfaces between two solids.

Most of the results for rare-gas layers can be transferred to other insulating adlayers, in particular if these are weakly bound (physisorbed) to metal surfaces. Strong chemical binding is usually accompanied by the formation of hybridized levels, which may lead to a complete quenching of the image-potential states. While the decoupling of image-potential states by adlayers with negative electron affinity can increase their lifetime up to several picoseconds,[32] the time scale for resonant charge transfer from a hybridized level of a strongly chemisorbed atom to a metal can be as short as some hundred attoseconds.[33]

The paper is organized as follows: In section 2, we describe the basic physics of image-potential states on metals and the influence of dielectric adlayers on their properties. This is followed by a short introduction to the technique of two-photon photoemission and to the preparation of well-ordered rare-gas layers (section 3). In section 4, we review the experimental work on the dynamics of image-potential states at rare-gas/metal interfaces. The corresponding microscopic models are discussed in section 5. Section 6 is devoted to the recent work on buried interface states at rare-gas/metal interfaces. The focus of this review will be on rare-gas layers, but we will also briefly discuss the work on the dynamics of image-potential states on organic layers in section 7.

2. Image-Potential States

2.1. Bare Metal Surfaces

Image-potential states owe their existence to the polarization of near-surface electrons by a charge that is placed in front of the surface. These normally unoccupied electronic surface states were first discussed by Cole and Cohen[34] and Shikin[35] for liquid helium, where they could be experimentally observed by microwave absorption spectroscopy.[36] The existence of image-potential states on metal surfaces was predicted by Echenique and Pendry[37,38] and has been confirmed first by inverse photoemission spectroscopy[39,40] and subsequently by two-photon photoemission using nanosecond lasers.[41] For a metal, the classical image potential has the form

$$V(z) = E_{vac} - \frac{e^2}{4z} \quad (1)$$

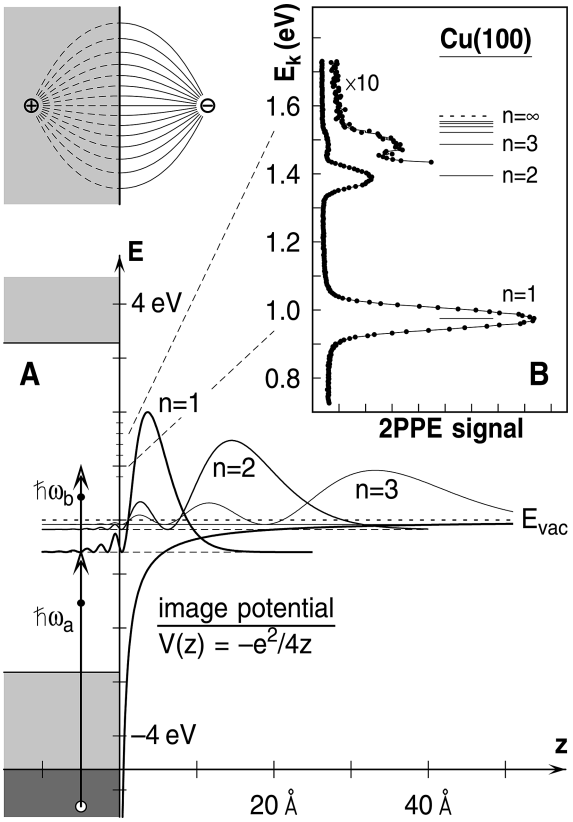

Figure 1. (A) Electric field and potential energy diagram of an electron in front of a Cu(100) surface ($z = 0$). The potential well formed by the sp band gap and the Coulomb tail leads to a series of discrete hydrogen-like electronic states that extend into the vacuum ($z > 0$). The squares of the wave functions of the lowest three states are shown. (B) Energy-resolved 2PPE spectrum obtained after excitation by photons of energy $\hbar\omega_a$ and $\hbar\omega_b$. The energy of the intermediate state E is related to the kinetic energy E_k by $E = E_k - \hbar\omega_b$. Reprinted with permission from *Science* (http://www.aaas.org), ref 8. Copyright 1997 American Association of the Advancement of Science.

with z denoting the distance from the surface. If the bulk band structure projected onto the surface has a gap near the vacuum energy, electrons can be trapped between the attractive image potential and the metal, and a series of hydrogen-like states with energies

$$E_n = E_{vac} - \frac{Ry}{16}\frac{1}{(n+a)^2} \quad (2)$$

is formed, where n is the quantum number, Ry is the Rydberg energy, and a is the quantum defect[37,42] (Figure 1). Electrons in image-potential states are only bound in the direction normal to the surface and can move almost freely in the parallel plane. Relaxation of electrons that are transiently excited into these states occurs predominantly via inelastic scattering with the metal electrons and creation of electron−hole pairs in the metal. In comparison to other electronic excitations at surfaces, image-potential states exhibit relatively long lifetimes, because they are located mainly in the vacuum region in front of the metal. The lifetime of the first image-potential state, for example, ranges from 10 to 60 fs,[7] depending on the substrate material and orientation. The lifetimes scale like $\tau \propto n^3$ in the limit of high quantum numbers n, as expected from the classical round-trip time.[8,37]

It is one of the most attractive features of image-potential states that it has become possible to measure their lifetimes with high accuracy by means of time-resolved 2PPE and at the same time to perform realistic many-body calculations of their decay.[7] Parallel to the development of a full theory, the so-called bulk penetration approximation has frequently been applied in the literature.[42,43] This model assumes that the lifetimes scale inversely to the probability density $p = \int_{-\infty}^{0}|\Phi(z)|^2\,dz$ of the electron inside the metal

$$\tau = \frac{\hbar}{p\Gamma_b} \quad (3)$$

where Γ_b, the line width of the bulk states, is an empirical parameter. The bulk penetration p depends on the energetic position of the image-potential states in the projected band gap. It has a minimum value of a few percent in the center of the gap and approaches unity at the upper and lower band edges, where the image-potential states are degenerate with bulk states. Examples for both cases are the $n = 1$ image-potential states on Cu(100) and Cu(111), which are located close to the center and the upper edge of the projected band gap, respectively. Their wave functions are plotted in Figure 2, which shows that, in addition to the larger bulk penetration on Cu(111), the maximum of the $n = 1$ wave function is shifted much closer to the surface compared to the case for Cu(100).

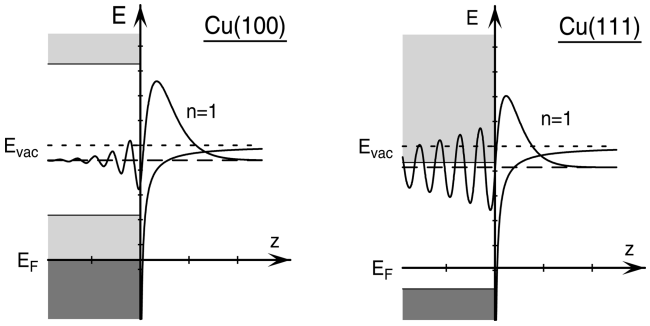

Figure 2. Schematic energy diagrams, image potential, and wave function of the $n = 1$ image-potential state in (a) Cu(100) and (b) Cu(111). The wave functions were obtained by solving the one-dimensional Schrödinger equation using a model potential.[48,157] Reprinted from ref 118, copyright 2005, with permission from Elsevier.

The bulk penetration approximation is motivated by the fact that the decay processes are mediated by the interaction with the bulk electrons. It neglects the nonlocal character of the Coulomb interaction, which plays an important role at surfaces due to the reduced screening and also due to the available phase space for the decay.[7,44,45] For this reason, penetration arguments alone are generally not sufficient to understand the decay of image-potential states at different surfaces, sometimes not even qualitatively. One striking example of the limitations of the penetration approximation appears when comparing Cu(100) and Ag(100) surfaces which have a very similar electronic structure. Due to a slightly smaller sp-gap, the penetration of the wave functions in Ag(100) is slightly larger than that in Cu(100), whereas the experimental decay rates of the image-potential states are nearly 40% smaller.[9] Only after properly accounting for the decay into the surface plasmon can many-body calculations explain the experimental trend.[46,47] Another example is provided by the first image-potential states of Cu(111) and Cu(100). While the measured lifetimes are 40 and 18 fs, respectively,[9,18,23,24] model-potential calculations give penetration values of 0.22 and 0.05.[48] Thus, the rates differ

by a factor of 2, while the penetrations differ by a factor of 4. In this case, it is the reduced phase space of available final states in Cu(111) and the presence of the occupied surface states in Cu(111), when accounted for in a many-body description, that give the correct ratios of lifetimes.[13,49] Nevertheless, the bulk penetration may be used to estimate the change of the lifetimes of particular surfaces in dependence on the thickness of an adsorbate layer. In particular, for rare-gas adsorbates on Cu(001) described in detail below, the penetration approximation appears to work very well.[32] For this surface, the nonlocal contributions to the total decay rate cancel out each other to a large extent.[10]

Most of the experiments with dielectric layers have been conducted with the noble metals Ag and Cu as substrate. With respect to the lifetime of image-potential states, the (001) surfaces of these metals represent the most simple situation. The vacuum level is located close to the center of the projected band gap, and the wave function of all members of the Rydberg series of image-potential states decays exponentially into the metal bulk. For the (111) surfaces, the vacuum level is located above the gap, and the $n = 2$ and higher image-potential states are degenerate with bulk states.[42] Thus, the lifetimes on the (111) surfaces are not only generally shorter than those on the (001) surfaces,[9,18,23,24,50,51] but also the $n = 2$ and higher states decay even faster than the $n = 1$ state.[23,51,52,53] Compared to the case of the surfaces of noble metals, the lifetimes of image-potential states on the surfaces of transition metals are shorter due the high density of d-electrons at the Fermi level.[14,15,48,54,55]

2.2. Influence of Dielectric Adsorbate Layers

In the presence of well-ordered adsorbates that do not introduce unoccupied electronic levels in the energy range of the image-potential states, the wave functions of the latter will retain their simple hydrogenic character.[56,57] Systems with such properties, that have been studied by time-resolved 2PPE, include Xe/Ag(111),[58,59] alkanes/Ag(111),[51,60] Xe and N_2/Cu(111),[17,53] Xe/Ru(0001),[61,62] and Ar/Cu(100).[32] Lifetimes have been found to increase by several orders of magnitude, depending on the thickness and the electronic properties of the layer.

The basic physics of decoupling of image-potential states by homogeneous insulating layers is already contained in a simple dielectric continuum description of the adlayers. The model goes back to the work by Cole,[34,63] who discussed the possibility of increasing the binding energy of image-potential states on the surfaces of liquid He, Ne, or H_2 by putting films of these materials on a metal substrate. The modified image potential given by Harris and co-workers[25,64] has the form

$$V_{in}(z) = E_{CBM} - \frac{e^2}{4\epsilon z} + ..., \quad (0 < z < d)$$

$$V_{out}(z) = \frac{-\beta e^2}{4(z-d)} + \frac{(1-\beta^2)e^2}{4\beta}\sum_{k=1}^{\infty}\frac{(-\beta)^k}{z-d+kd}, \quad (z > d) \quad (4)$$

where z is the distance from the metal, d is the layer thickness, ϵ is the dielectric constant of the adlayer, and $\beta = (\epsilon - 1)/(\epsilon + 1)$. E_{CBM} denotes the position of the conduction band minimum with respect to the vacuum level, that is, the affinity level of the rare gas layer. It is related to the electron affinity EA by $E_{CBM} - E_{vac} = -EA$. V_{out} is the potential in the vacuum region outside of the layer. The first term is the image potential outside an infinite dielectric, and the second term is a series of corrections that arises from the presence of the metal and the finite layer thickness. In particular for a thin layer, V_{out} is even dominated by the image-potential of the metal. The potential inside the dielectric, V_{in}, is the screened image potential of the metal, which is lowered or raised with respect to the vacuum level depending on the electron affinity of the adlayer. (The complete form of V_{in} that results from the solution of the Poisson equation was first given in ref 65. $V_{in}(z) = V_{CBM} - e^2/4\epsilon z + (e^2/4\epsilon)\sum_{k=1}^{\infty}(-\beta)^k[2/kd - 1/(kd - z) - 1/(kd + z)]$. The summation arises from image charges caused by the finite layer thickness d.)

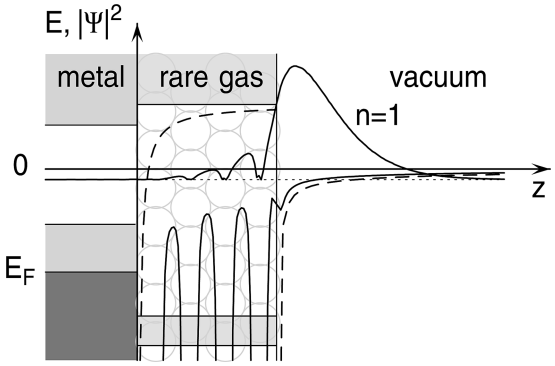

Figure 3. Schematic energy diagram of a rare-gas spacer layer on a metal substrate along with the probability density of the $n = 1$ image-potential state. The wide band gap of the insulating film leads to an out-shift of the probability density away from the metal. The potential inside the film arising from the individual layers is highly corrugated (solid line). Also shown is the potential of the dielectric continuum model (dashed line). Electronic bands are marked as shaded regions. Reprinted Figure 1 from ref 57, copyright 2004, with kind permission of Springer Science and Business Media.

The effect of the adlayer on the image-state properties depends critically on the position of the affinity level E_{CBM}. If $E_{CBM} > E_{vac}$, that is, for negative electron affinity, as in the case of Ar, N_2, or alkanes, the adlayer represents a tunnel barrier for an electron in an image-potential state and its wave function will be pushed into the vacuum outside of the layer (Figure 3). Its binding energy will be mainly determined by V_{out}, whereas the potential V_{in} describes the form of the tunneling barrier that determines the penetration of the wave function to the metal substrate and, thus, the lifetime. The longest lifetime of an image-potential state that has been measured so far with 2PPE is 10 ps for the $n = 1$ state of Cu(100) in the presence of five monolayers of Ar.[32] Even longer lifetimes can be expected for thicker films, but the vanishing overlap with the metal electrons not only suppresses the inelastic decay but also prevents an optical excitation and, therefore, the observation by 2PPE. Indeed the first experimental observation of image-potential states on liquid helium revealed lifetimes of hours.[36] In the case of $E_{CBM} < E_{vac}$, the energy levels of the image-potential states can become degenerate with the conduction band of the adlayer and the wave functions of the states penetrate the layer. Examples are the $n \geq 2$ states in the presence of the rare gases Xe and Kr. In this case, a quantum-well-like behavior with an oscillatory dependence of energy and lifetime on layer thickness is found.[52,57]

A special effect, that is already contained in the dielectric continuum model, is important for Cu(111) and Ag(111).

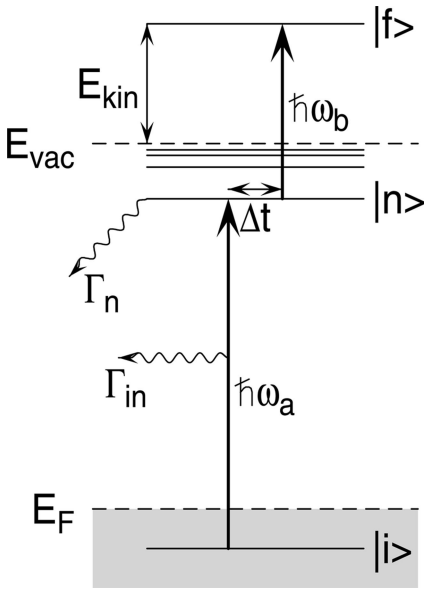

Figure 4. Schematic energy diagram for a two-color 2PPE excitation scheme.

The image-potential states lie close to the upper edge of the band gap on these surfaces. The drop of the work function upon rare-gas adsorption shifts the states away from the band edge, resulting in a reduced penetration into the bulk. This effect contributes to some extent to the lifetime increase after monolayer adsorption on these surfaces.[17] In the case of Cu(100) and Ru(0001), this mechanism is negligible, because the image-potential states lie close to the center of the gap.

Whereas the dielectric continuum model can explain the influence of adlayers in a qualitative way, recent work has shown that it is not sufficient for a satisfactory quantitative description. Hotzel *et al*. have used a momentum dependent effective mass $m^*(z)$, to model the coverage dependence of energies and lifetimes for the system Xe/Cu(111).[53] Gaffney and co-workers applied the two-band model of nearly free electrons for describing the electronic structure of aromatic overlayers on Ag(111).[66] Berthold *et al*. showed that for Xe/Ru(0001) the properties obviously depend on the morphology of the adlayer.[62] In the case of Ar/Cu(100), the continuum model fails to predict the correct binding energy for monolayer coverage. At the same time, it underestimates the lifetime for thicker layers.[32] Most of these deficiencies of the dielectric continuum can be fixed by including the atomic corrugation of the adlayer as discussed in section 5.1.

3. Experimental Techniques

3.1. Time-Resolved Two-Photon Photoemission

Time-resolved two-photon photoemission (2PPE) is a pump−probe technique that combines laser excitation with photoelectron spectroscopy.[8,50,67−76] A first laser pulse with photon energy $\hbar\omega_a$ excites metal electrons from an initial state $|i\rangle$ below the Fermi level E_F into a normally unoccupied state $|n\rangle$ with energy E_n between E_F and the vaccum energy E_{vac} (Figure 4). A second laser pulse $\hbar\omega_b$ follows after a controlled time delay Δt and lifts a part of the excited electrons in an final state $|f\rangle$ above the vacuum energy. The photoelectrons escape from the sample with the kinetic energy $E_{kin} = \hbar\omega_b - E_B$, where $E_B = E_{vac} - E_n$ is the binding energy and is detected by means of a time-of flight or dispersive electron spectrometer. If pump and probe pulses are overlapping in time, the 2PPE signal can also originate from occupied states which are photoemitted by a coherent two-photon excitation process via a virtual intermediate state. Different excitation pathways can be discriminated by their different dependences on photon energies. The time evolution of the transiently excited electrons is probed by recording the 2PPE signal as a function of the time delay between the pump and probe pulses with the spectrometer set to a fixed energy. The inelastic lifetimes τ can be obtained directly from the exponential decay of the time-resolved 2PPE curves. In the case that several close lying states such as image-potential states are simultaneously excited within the bandwidth of the short pump laser pulse, the 2PPE signal shows a beating with the frequency difference of the intermediate states as a function of the time delay. Such quantum-beat spectroscopy of image-potential states[8,11,12,32,57,77] provides not only an accurate measure of the energy separation of the states. The comparison of the decay of the oscillations with the overall decay of the 2PPE signal directly reflects quasielastic scattering processes which result in a loss of phase correlation between their wave functions.[11,12,77]

A complete description of the dynamics of the 2PPE process has to include not only the dynamics of the populations but also those of the coherence (optical polarizations) between the different electronic states, which are induced by the optical excitations. This can be done by applying a density-matrix formalism[8,9,16,23,74,77−82] where the interaction with the enviroment is empirically described by the introduction of rates for the decay of the populations due to inelastic scattering $\Gamma_n = 1/\tau$ and for the dephasing of the optical polarizations Γ_{in} (and Γ_{nf} as well as Γ_{if}[83]) that can decay by inelastic as well as by elastic scattering. The inelastic lifetimes of the initial and final states are usually assumed to be infinite ($\Gamma_i = \Gamma_f = 0$). As long as $\hbar\Gamma_{in}$ is large compared to the experimental energy resolution given by the detector resolution and the bandwidth of the probe pulses, it can also be determined in the frequency domain by measuring the line width of the photoemission peak for large delays between pump and probe pulses if inhomogeneous broadening can be neglected and the laser pulse form is known.[82] In the limit of a fast dephasing rate Γ_{in} and, in particular, for long lifetimes as observed for the rare-gas covered surfaces, the population dynamics can be described also by a simple rate-equation model only for the populations, which yields the inelastic decay rate Γ_n of the intermeditate state.

For well ordered crystals, 2PPE conserves the momentum of electron motion parallel to the surface. It can be computed from the knowledge of the emission angle φ by using $k_{||}$ (Å^{-1}) $= 0.5123[E_{kin}$ (eV)$]^{1/2}$ sin φ, permitting momentum-resolved studies. Image-potential states show a free-electron-like parabolic dispersion parallel to the surface, which can be parametrized as

$$E = E_0 + \frac{\hbar^2 k_{||}^2}{2 m_{eff} m_0} \qquad (5)$$

where m_{eff} is the effective mass, m_0 is the mass of the free electron, and E_0 is the energy of the surface band for $k_{||} = 0$.

3.2. Preparation of Well-Ordered Rare-Gas Layers

For the comparison with theoretical predictions, it is important to conduct the experiments with lateral homogeneous layers that contain a minimum of defects. It has been

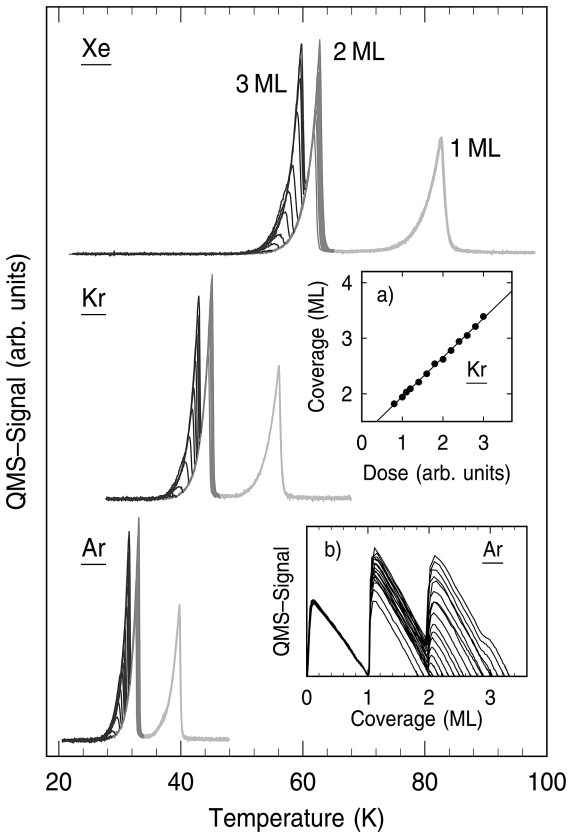

Figure 5. TPD spectra of Ar, Kr, and Xe layers obtained by dosing on top of annealed monolayers adsorbed on Cu(100) (see text). Initial coverages range from 1.7 to 3.4 ML, and the heating rate was 0.5 K/s. (a) Calibration curve for Kr. (b) Plot of the Ar data as a function of sample coverage during thermal desorption (layer plot; see ref 89). The sharp signal dips at 1, 2, and 3 ML demonstrate layer-by-layer desorption of the films. Between the curves, the initial coverage was varied as stated above. Reprinted Figure 2 from ref 57, copyright 2004, with kind permission of Springer Science and Business Media.

shown that steps and defects not only result in an increased line width of image-potential states by dephasing[11,12,84] but that they also lead to faster temporal decay by enhanced intraband and interband scattering.[19,22,24,85−87]

In the case of rare-gas layers, the experimental technique for the preparation of well-ordered atomically flat layers is well developed. It can be achieved by employing the unique properties of temperature-programmed desorption (TPD).[88,89] As shown in Figure 5 for rare-gas layers on Cu(100), desorption of the individual layers gives rise to sharp, clearly separated peaks with zero-order desorption kinetics up to the third monolayer (ML). By comparing the temperature-integrated signal with the peak area of 1 ML, the initial coverage can be measured. The growth of a defined number of layers can be achieved with high reproducibility by dosing a controlled amount of the rare gases through a microchannel plate.

Perfect, annealed monolayers are easily obtained by slightly overdosing the sample and removing the excess coverage by ramping the sample temperature just beyond the 2 ML peak. The preparation of highly ordered thick films involves two more steps. At first, an annealed monolayer is made, on which subsequently a certain number of further layers are adsorbed. Only under this condition can layerwise desorption be observed in the TPD spectra (see inset b of Figure 5). Final annealing of the sample to temperatures

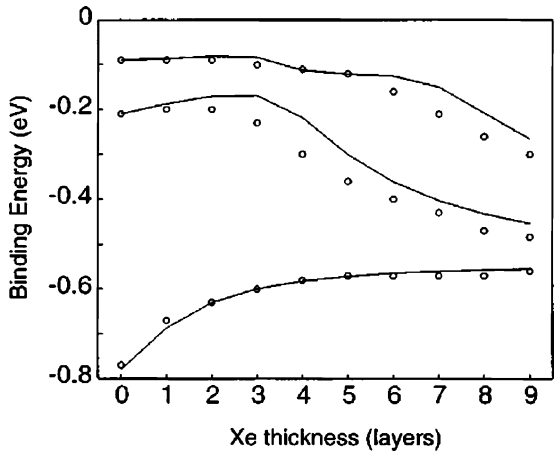

Figure 6. Experimental binding energies relative to the vacuum level for the $n = 1$, 2, and 3 image-potential states for Xe overlayers on Ag(111) (symbols) and predictions (lines) of the modified dielectric continuum model. Reprinted with permission from ref 64. Copyright 1996 American Institute of Physics.

below the multilayer desorption peak results in layer smoothing by rapid intra- and interlayer diffusion and simultaneously avoids desorption.

4. Decoupling by Rare-Gas Adlayers

4.1. Xe/Ag(111)

The first 2PPE experiments on image-potential states of adsorbate covered metal surfaces were performed by Harris and co-workers. Padowitz *et al*. have shown that image-potential states may persist in the presence of Xe and alkane overlayers.[56] They have observed a decrease of the binding energy of the $n = 1$ image-potential state upon absorption of a Xe monolayer. Furthermore, the effective mass has been observed to decrease toward the value of the free electron. Both effects were attributed to the repulsion of the $n = 1$ wave function away from the attractive metal surface.[90] McNeill *et al*. studied the binding energy and effective mass of the $n = 1-3$ states systematically as a function of film thickness for Xe/Ag(111).[64] As shown in Figure 6, a completely different behavior has been observed for $n = 1$ on the one side and for $n = 2$ or 3 on the other side. Whereas the binding energy of the $n = 1$ state decreases with Xe coverage, it increases for $n = 2$ and $n = 3$. This can be understood by considering the positive electron affinity of 0.5 eV of Xe. The $n = 1$ state remains below the conduction band minimum of the Xe layer up to 9 ML, which results in a partial decoupling from the attractive image-potential of the metal. The $n = 2$ and $n = 3$ states are degenerate with the conduction band of Xe and can penetrate into the layer, which increases their binding energy. In a subsequent time-resolved study, McNeill *et al*. have shown that the different degree of penetration is also reflected by the inelastic lifetime of the image-potential states. While the lifetime of the $n = 1$ state increases monotonically with Xe layer thickness due to the decoupling from the metal, the lifetimes for $n = 2$ and $n = 3$ show an oscillatory dependence. Whenever a half-cycle of the wave function fits into the layer, the penetration, and, therewith, the coupling to the metal, is enhanced, which reduces the lifetime considerably. The influence of the Xe adlayers on binding energies and lifetimes could be qualitatively described by the dielectric continuum model. The quantum-well character of the penetrating $n = 2$, 3 states,

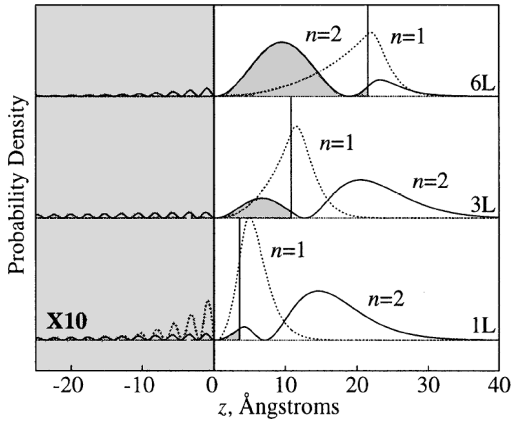

Figure 7. Calculated probability density for the $n = 1$ and $n = 2$ states for 1, 3, and 6 ML of Xe. Reprinted (Figure 3) with permission from ref 52 (http://link.aps.org/abstract/PRL/v79/p4645). Copyright 1997 The American Physical Society.

however, could not be well reproduced, because the dielectric continuum model treats the adlayer as a homogeneous dielectric without internal electronic structure.

To account for the conduction band of the Xe adlayer, McNeill *et al*. have described the potential inside the Xe layer as a flat band with an effective mass obtained from a quantum-well analysis.[64] The effective mass for motion parallel to the surface has been shown to decrease with Xe layer thickness down to 0.6 of the free electron mass for $n = 1$ at four layers of coverage. This decrease toward the literature value of 0.35[91,92] for the bulk Xe conduction band demonstrates that the wave function of the electron is confined to a large extent within the Xe layer. Figure 7 shows the probability density of the $n = 1$ and $n = 2$ states for 1, 3, and 6 ML of Xe calculated within the flat-band approximation for the potential inside the layer. Whereas the $n = 1$ state shifts further away from the metal for increasing thickness, the $n = 2$ state penetrates into the Xe layer, in particular if the Xe layer terminates near a node of the wave function, as can be seen for three layers, and, even more pronounced, for six layers, in contrast to the single layer. This results in an oscillatory enhancement of the overlap with the Ag bulk states and, therewith, in an increase of the binding energy and a decrease of the lifetime.

4.2. Xe/Cu(111)

Wolf *et al*. have studied Xe/Cu(111),[17,53] which is very similar to Xe/Ag(111). As in Ag(111), the $n = 1$ state is located near the top of the projected band gap of Cu(111) while the $n = 2$ state lies above the gap, which results in a shorter lifetime of $n = 2$ compared to $n = 1$. Adsorption of a monolayer of Xe reduces the work function by 0.5 eV. This shifts the $n = 1$ state further away from the upper edge of the band gap, which accounts to a certain extent for the observed increase in lifetime. Furthermore, the wave function is decoupled from the metal since the Xe layer acts as a tunnel barrier for the $n = 1$ state. For $n = 2$ the change of the work function is not sufficient to shift this state below the top of the gap. It remains degenerate with the Xe conduction band, which results in only slight changes of binding energy and lifetime (Figure 12). As on Ag(111), the lifetime of the $n = 2$ state has a maximum at 2 ML due to its quantum-well character and remains still shorter than that for $n = 1$ due to the enhanced coupling to the metal. The results have been discussed within the dielectric continuum model, whereas the influence of the electronic structure of the Xe adlayer was taken into account by using a momentum dependent effective mass.

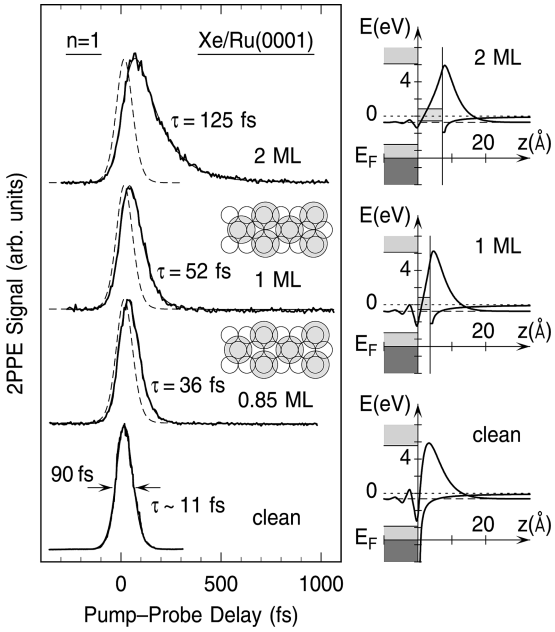

Figure 8. Left: Lifetime measurements of the $n = 1$ state of Ru(0001) for various Xe coverages. Right: Schematic energy diagrams and wave functions as computed with a tunneling model. The coverage of 0.85 ML corresponds to the commensurate $(\sqrt{3}\times\sqrt{3})$-R30° superstructure, and 1 and 2 ML correspond to the incommensurate monolayer and bilayer, respectively. The dashed curves reproduce the results of the clean surface for comparison. Adapted from ref 62.

4.3. Xe/Ru(0001)

The binding energies and, in particular, the lifetimes of the image-potential states on Ag(111) and Cu(111) depend strongly on the position of the vacuum level relative to the projected band gap. To isolate the effect of decoupling of Xe layers from the shift of the work function, Berthold *et al*. have studied Xe/Ru(0001).[62] Ru(0001) has a large band gap of 9.4 eV. The vacuum level and, with it, the image-potential states are located close to the center of the projected band gap, which makes their properties insensitive to shifts of the work function. Xe adsorption was found to lead to an increase of the lifetime for $n = 1$ and even for $n = 2$ despite its penetration into the Xe layer. However, the lifetime of the $n = 2$ state exhibits a weaker dependence on Xe coverage. In addition, this study could demonstrate the influence of the morphology of the adsorbate on the lifetime of the image-potential states. Xe/Ru(0001) shows two well-characterized phases of the adlayer geometry. At a coverage of $\theta = 0.85$ ML, a commensurate $(\sqrt{3} \times \sqrt{3})$R30° superstructure is observed, whereas the full monolayer is incommensurate,[93] as illustrated in the insets of Figure 8. These changes in the geometric structure of the adlayer have a significant influence on the coupling properties of the image-potential states. The two monolayer phases were observed to differ distinctly in the lifetimes of the first image-potential state, which amount to 36 fs for the commensurate monolayer and 52 fs for the incommensurate monolayer. The shorter lifetime for the commensurate phase has been explained by the enhanced Xe/Ru interaction. Creation of a theoretical model of this effect would be a demanding task, because it involves a three-dimensional description of the

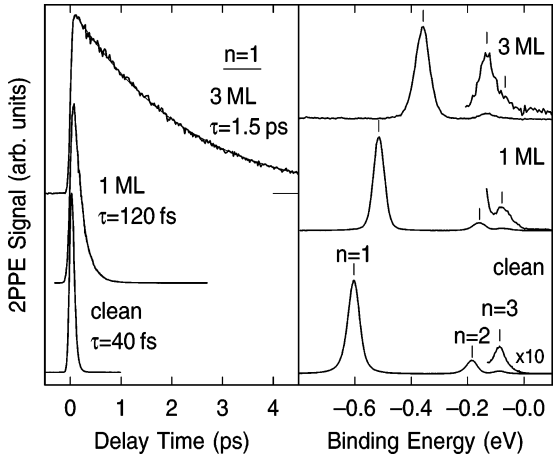

Figure 9. Pump−probe traces (left) and 2PPE spectra (right) for clean Cu(100) and for Ar coverages of 1 and 3 ML. Reprinted (Figure 2) with permission from ref 116 (http://link/aps.org/abstract/PRL/v89/p046802). Copyright 2002 The American Physical Society.

adsorbate/metal system. Due to the large complexity introduced by the strong Xe/Ru coupling and by the large number of electrons in the Xe atom, such a calculation is still missing. However, for weakly interacting Ar layers on a noble-metal surface, a truly three-dimensional theory is feasible, as will be discussed in section 5.3.

4.4. Ar,Kr,Xe/Cu(100)

The influence of the electron affinity of the rare-gas layers on the properties of the image-potential states has been systematically studied by Berthold *et al*. in a subsequent work.[57] In this study, binding energies and lifetimes for Xe, Kr, and Ar layers on Cu(100) have been compared for coverages up to 5 ML. Quantum-beat spectroscopy[8] has been additionally used to determine binding energies up to $n = 5$ and lifetimes up to $n = 4$ at coverages of 0−2 ML. As for Ru(0001), the vacuum level of Cu(100) is located close to the center of the projected band gap. Thus, the potential barrier at the metal/rare-gas interface is almost constant within the range of binding energies of the image-potential states, and shifts of the work function do not interfere with the decoupling effect of the rare-gas layers.

In contrast to Xe and Kr, Ar has a negative electron affinity which leads to a strong repulsion of the whole series of image-potential states from the metal. 2PPE data for the clean surface and the Ar-covered surface are shown in Figure 9. The states $n = 1$ to $n = 3$ are fairly well resolved on all films. The repulsion from the metal results in a decrease of the binding energy of all image-potential states and a strong increase of the lifetime as a function of Ar thickness. The 2PPE intensity showed pronounced coverage-dependent oscillations. For 2 ML of Ar, for example, the $n = 1$ intensity is 200 times weaker than that for 1 ML and three times less than that for 3 ML, which is most likely governed by a variation of the optical matrix elements for the second photoemission step with layer thickness, since the continuum wave functions above the vacuum level will be also affected by the presence of the rare-gas layers.

In the case of Xe and Kr, only the lifetime of the $n = 1$ state increases monotonically with coverage, but this increase is much less pronounced than in the case of Ar. The lifetime of the $n = 2$ state first increases, but then it reaches a maximum for a coverage of 2 ML. At 4 ML, the lifetimes

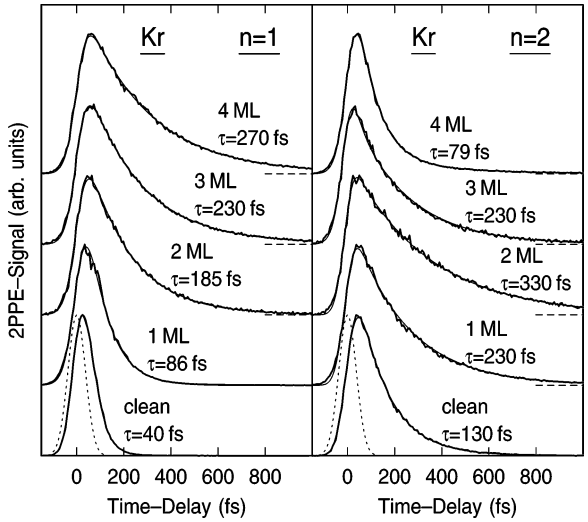

Figure 10. Time-resolved pump−probe traces of $n = 1$ and 2 for 0−4 ML of Kr/Cu(100). Thin lines are fits using a rate-equation model. Dotted lines indicate the experimental time resolution. Reprinted Figure 6 from ref 57, copyright 2004, with kind permission of Springer Science and Business Media.

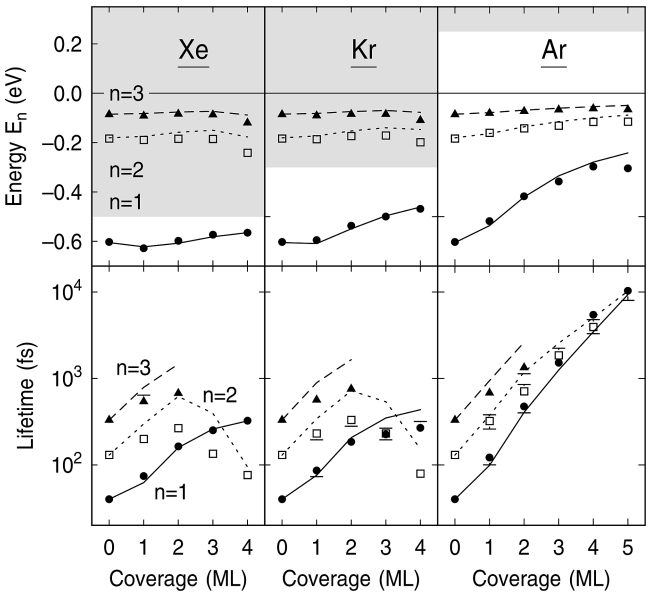

Figure 11. Lifetimes (bottom) and energies (top) of the first three image-potential states as a function of coverage for Xe, Kr, and Ar on Cu(100). Experimental values are shown as symbols. The thin lines depict the results of model calculations as described in section 5.1. Conduction bands of the rare gases are indicated by shading. Reprinted Figure 7 from ref 57, copyright 2004, with kind permission of Springer Science and Business Media.

drop even below the value of the clean surface. The corresponding 2PPE data for Kr are plotted in Figure 10. The Xe data are very similar.

Figure 11 summarizes the results for binding energies and lifetimes. It clearly shows the influence of the electron affinity, that is, the position of the conduction band minimum E_{CBM} of the rare-gas layer. As long as an image-potential state is located below E_{CBM}, the adlayer represents a tunnel barrier and the wave function is decoupled from the metal surface. Thus, the binding energy decreases and the lifetime increases almost exponentially with layer thickness, as can be seen for the $n = 1$ state on Xe and Kr and for the whole Rydberg series of image-potential states on Ar. This effect increases systematically with increasing E_{CBM}, that is, with

increasing height of the tunnel barrier, from Xe to Kr and Ar ($E_{vac} - E_{CBM} = -0.5$ eV, -0.3, and $+0.25$ eV, respectively). For Ar, this leads to an increase of the lifetime by a factor of 10 if the layer thickness is tripled and reaches up to 10 ps at 5 ML for $n = 1$.[32] As the binding energy and, therewith, the distance to the affinity level of $n \geq 2$ is smaller in comparison to the case for $n = 1$, the tunneling barrier is lower and the lifetimes increase less rapidly compared to the case for $n = 1$.

Xe and Kr layers are slightly attractive to electrons and represent a barrier only for the lowest $n = 1$ state. The higher quantum states $n \geq 2$ are degenerate with the Xe or Kr conduction band. Hence, they can penetrate the layer that acts like a quantum well, as in Xe/Ag(111) and Xe/Cu(111). Every time the layer thickness matches one-half-cycle of the oscillating wave function, a resonance is formed with a high probability amplitude near the metal, which leads to a resonant decrease of the lifetime as well as to an increase of the binding energy. For Xe and Kr on Cu(100), the quantum-well resonance is formed for 4 ML. At 2 ML, the resonance condition is least fulfilled, which causes the initial increase in lifetime of the $n = 2$ state and similarly of the $n = 3$ state.

As discussed by Berthold *et al*.,[57] the coverage dependence of binding energies and lifetimes can be basically described by the previously mentioned dielectric continuum model.[25,64] The quantum-well-like behavior of the $n \geq 2$ states in Xe and Kr, however, cannot be well reproduced. A modification of the dielectric continuum model which describes the potential inside the layer V_{in} as a flat band[64] can reproduce the quantum-well resonance in Kr at 4 ML but overestimates the lifetime by up to a factor of 30. Even if the agreement with the experimental data is better in other cases, the dielectric continuum model and its variants[53] are not based on a microscopic description of the electronic structure of the rare-gas layers and depend on empirical parameters which have no physical meaning. The electronic structure of the adsorbate layers enters into these continuum models only via the electron affinity or sometimes by introducing an effective mass.[64,53] This simplification may be justified in the limit of very thick films. In the case of films consisting of only a few monolayers, however, the discrete structure of the atomic layers must be considered.

A more realistic description of the electronic structure of the adsorbate layer has been given by Berthold *et al*.[57,94] They developed a microscopic one-dimensional model potential as described in section 5.1. It is composed by a superposition of the image-potential with a potential that has the periodicity of the rare-gas ions perpendicular to the surface. This potential naturally produces the conduction band of the rare-gas crystal without the neglect of the image-potential as in a flat band model.

4.5. N_2/Cu(111)

In their study of Xe/Cu(111), Wolf and co-workers have also reported about N_2/Cu(111).[53] In contrast to Xe, N_2 has a negative electron affinity which has been estimated to be between -1 and -2 eV. The negative electron affinity affects the properties of the image-potential states in a similar way as for Ar/Cu(100), where it is responsible for a strong repulsion of all image-potential states away from the metal. The binding energy of the $n = 1$ state on N_2/Cu(111) was found to decrease more strongly compared to that on Xe/Cu(111), and in particular, the lifetime of the $n = 1$ state grows by more than 1 order of magnitude per monolayer (Figure 12). Also, the lifetime of $n = 2$ strongly increases upon monolayer adsorption but remains below the one of $n = 1$, since the energy of $n = 2$ is still close to the sp-band edge of Cu(111). This results in a larger bulk penetration and, therewith, a shorter lifetime compared to the case of $n = 1$.

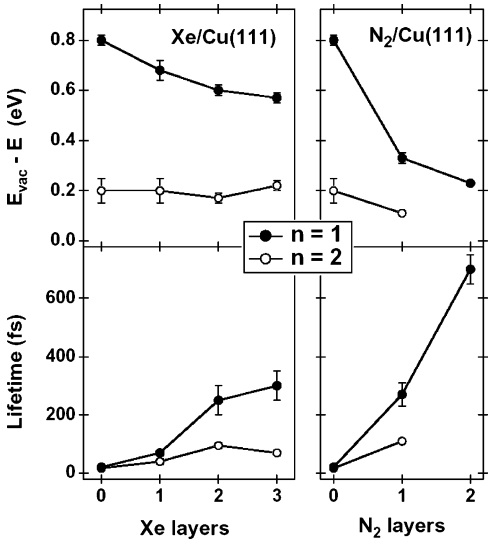

Figure 12. Lifetimes and binding energies of the $n = 1$ and 2 image-potential states as a function of number of Xe (left) and N_2 (right) layers on Cu(111). Reprinted Figure 2 from ref 53, copyright 1999, with kind permission of Springer Science and Business Media.

4.6. Heterolayers

Hotzel *et al*. have studied heterolayers of molecular adsorbates (O_2 and N_2) physisorbed on top of Xe spacer layers on Cu(111).[95,96] The goal was to study electron transfer into a molecular resonance. However, the time scale of the electron transfer dynamics for molecules chemisorbed on metal surfaces is usually too fast to observe directly by 2PPE in the time domain.[97−99] The determination of lifetimes much shorter then 10 fs requires techniques which work in the frequency domain, like high-resolution spectroscopy of the Auger decay of core-excited states.[33,100] Therefore, many researchers have sought to reduce and control the coupling of adsorbate-induced states to the bulk metal by introducing thin insulating spacer layers.[101−108]

As discussed in the last section, the negative electron affinity of N_2 leads to a strong decoupling of the image-potential states from the Cu(111) surface. Insertion of a Xe spacer layer shifts the wave function further away from the metal, and an increase of the lifetime of the $n = 1$ image-potential state to 1.6 ps has been found for 1 ML of N_2 on top of 1 ML of Xe on Cu(111).[96] Angle-resolved measurements revealed a strong dependence of the inelastic decay rate on the parallel momentum. Due to the small decay rate at $k_{||} = 0$, electron−electron interaction has been excluded as the underlying mechanism for this intraband relaxation in contrast to the cases of Xe on Ag(111)[59] and to the interface states in Ar/Cu(100).[109] Instead, it has been suggested that the intraband scattering is linked to the excitation of low-energy phonons.

For O_2/Xe/Cu(111), a single unoccupied O_2 induced state has been found in the 2PPE spectra at 4 eV above E_F.[95] It has been brought in connection to the lowest-lying negative-

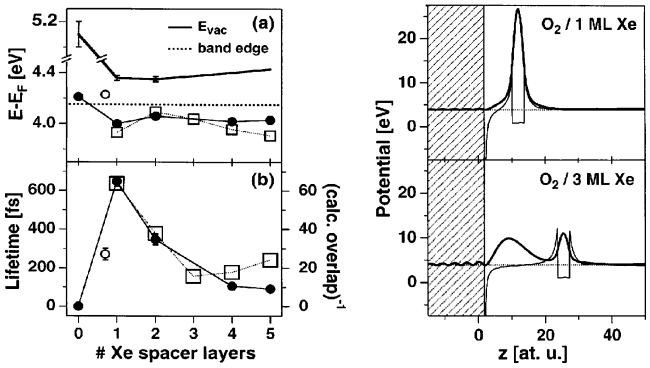

Figure 13. Energy (a) and lifetime (b) of the O_2-induced unoccupied state for 1 ML of O_2/Xe/Cu(111) as a function of the number of Xe space layers. Full circles: experimental data. Open squares: results of the model calculations for energy and inverse overlap with the Cu bulk, which is approximately proportional to the lifetime. (c) Model potential (thin line) and calculated probability density of the lowest-lying bound state (thick line) for O_2 on top of 1 and 3 Xe space layers, respectively. The same scale is used in both cases. Reprinted from ref 95, copyright 1998, with permission from Elsevier.

ion resonance X $^2\Pi_g$ of O_2, which corresponds to the population of an antibonding π^* orbital with an additional electron. However, the polarization dependence of the 2PPE intensity revealed a σ-symmetry which is compatible with an image-potential state. Also, its effective mass close to the mass of the free electron is typical for an image-potential state. Therefore, it has been proposed that the observed state results from the modification of the image potential by the presence of the O_2 molecule with its attractive negative-ion resonance. Even if O_2 is physisorbed on the bare Cu(111) surface, this state shows a very short lifetime of <10 fs. A huge increase of the lifetime to (650 ± 30) fs for one Xe spacer layer has been found. However, the addition of further Xe spacer layers led to a decrease of the lifetime again down to (90 ± 10) fs for five Xe layers (Figure 13b). This can be qualitatively understood by the fact that, in contrast to the $n = 1$ image-potential state on Xe/Cu(111) without O_2, the O_2 induced state is degenerate with the conduction band of bulk Xe. Thus, the Xe spacer layer does not represent a tunnel barrier. Nevertheless, for one Xe layer, the lifetime of the O_2 induced state is 1 order of magnitude longer than that of the corresponding $n = 1$ image-potential state. This behavior could be reproduced by model calculations using a one-dimensional potential in which the Xe layer is described within the dielectric continuum model and the negative-ion resonance of O_2 is represented by a square well with a centrifugal barrier (Figure 13c). Clearly, the penetration of the wave function in the Xe layer is stronger for 3 ML of Xe compared to a single space layer.

5. Microscopic Models

5.1. 1D Model Potential

As mentioned above, Berthold *et al.*[57,94] developed a one-dimensional model potential for the description of image-potential states on a rare-gas covered metal surface. In contrast to the dielectric continuum model, it takes into account the high corrugation of the potential inside the adsorbate layer due to the screened ion cores of the rare-gas atoms but keeps its simple one-dimensional character. The resulting model potential for the whole system $V(z)$ contains three parts

$$V(z) = V_{\mathrm{met}}(z) + V_{\mathrm{in}}(z) + V_{\mathrm{out}}(z) \tag{6}$$

which describe the potential within the metal, inside the rare-gas layer, and in front of the adlayer, respectively. Inside the metal, the well-known two-band model of nearly free electrons has been used

$$V_{\mathrm{met}}(z) = -\Phi - V_0 + 2V_{\mathrm{g}} \cos\left(\frac{2\pi}{d_{\mathrm{met}}}\left(z - \frac{d_{\mathrm{met}}}{2}\right)\right), \quad z \le 0 \tag{7}$$

Here, Φ denotes the work function, and d_{met} is the layer spacing normal to the surface. The offset V_0 and the potential strength V_{g} were adjusted to reproduce the positions of the lower and upper edges of the Cu(100) band gap. Inside the rare-gas layer of thickness d and in the vacuum region, the dielectric continuum model in the form given in ref 51 was used, where the constant conduction band minimum E_{CBM} (compare eq 4) was replaced by a one-dimensional corrugated potential $V_{\mathrm{atom}}(z)$

$$V_{\mathrm{in}}(z) = V_{\mathrm{atom}}(z) - \frac{e^2}{4\epsilon z} + \frac{e^2\beta}{4\epsilon(d-z)} - \frac{e^2\beta(d+2z)}{4\epsilon d(d+z)} + \delta V_{\mathrm{in}}(z), \quad 0 < z \le d \tag{8}$$

$$V_{\mathrm{out}}(z) = -\frac{e^2}{2(\epsilon+1)z} - \frac{e^2\beta}{4(z-d)} + \delta V_{\mathrm{out}}(z), \quad z > d \tag{9}$$

Here, $\beta = (\epsilon - 1)/(\epsilon + 1)$. $\delta V_{\mathrm{in}}(z)$ and $\delta V_{\mathrm{out}}(z)$ are higher order corrections, as described in detail in ref 57. The corrugated potential $V_{\mathrm{atom}}(z)$ describes the main features of the rare-gas band structure, which are a delocalized conduction band and a localized valence band. It is given by

$$V_{\mathrm{atom}}(z) = V_{\mathrm{bg}} - \sum_{i=1}^{n_{\mathrm{rg}}} V_{\mathrm{core}} \exp\left[\frac{-|z - d_{\mathrm{rg}}(i - {}^1/_2)|}{l_{\mathrm{scr}}}\right] \tag{10}$$

where l_{scr}, d_{rg}, and n_{rg} are the screening length, the layer spacing, and the number of atomic layers, respectively. The screening length determines the range of the atomic potential. It has only a minor influence on the computational results and was set to $l_{\mathrm{scr}} = 0.05 d_{\mathrm{rg}}$. The potential offset V_{bg} and the potential strength V_{core} were adjusted to reproduce the correct position and effective mass of the rare-gas conduction band minimum. Binding energies and wave functions have been computed by numerically solving the stationary Schrödinger equation for this potential. Examples of the potential and probability densities for Xe and Ar layers on Cu(100) are depicted in Figure 14. The potential oscillates inside the metal and the adsorbate layer with the period of the respective lattice constant, while its envelope follows the screened image potential of the continuum model. The stronger attraction inside the Xe layer compared to Ar is clearly visible. The probability density of the $n = 1$ state penetrates more strongly into the Xe than into the Ar layer, which reflects the different energetic positions relative to the conduction band minimum of the rare-gas crystal in both cases. The model can reproduce the quantum-well resonance of $n = 2$ at 4 ML of Xe, where the probability density inside the layer and the metal of $n = 2$ even exceeds the one of $n = 1$. This results in a shorter lifetime of $n = 2$ compared to $n = 1$ at this coverage. In the case of Ar, on the contrary,

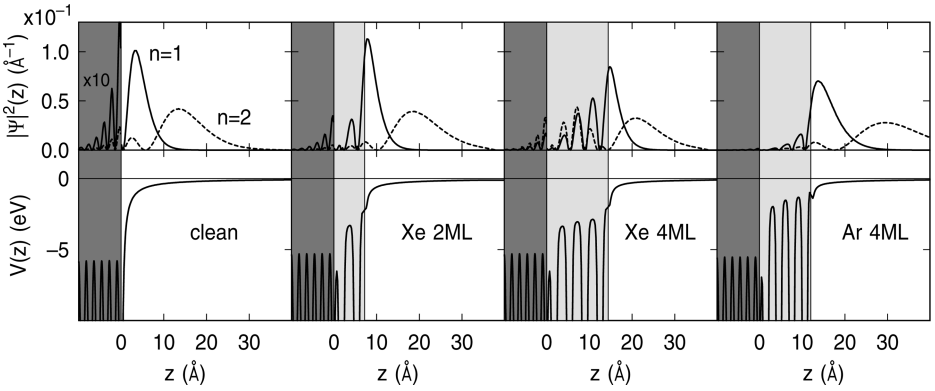

Figure 14. Examples of the atomic potential (bottom) along with the computed probability densities of $n = 1$ and 2 for clean Cu(100), 2 and 4 ML of Xe, and 4 ML of Ar. Metal and rare-gas films are highlighted in dark and light gray, respectively. Reprinted Figure 9 from ref 57, copyright 2004, with kind permission of Springer Science and Business Media.

the probability density decays exponentially inside the layer, which generates the tunneling-like coverage dependence.

Lifetimes for the rare-gas covered surface were calculated within the bulk-penetration approximation by scaling the experimental lifetimes of the clean surface with the computed probability density inside the metal. As discussed in section 2.1, this approximation neglects the nonlocal character of the decay mediated by the screened Coulomb interaction with bulk electrons.[10,45] However, recent many-body calculations of absolute lifetimes for Ar/Cu(100) (cf. section 5.2) show that the nonlocal contributions to the inelastic line width cancel each other to a large extent, as they do for the clean surface.[27]

The results of these model calculations for binding energies and lifetimes for Xe, Kr, and Ar on Cu(100) are depicted by the thin lines in Figure 11. They show very good agreement with the measured data. In particular, the binding energies are very well reproduced. Even the slight energy decrease of $n = 2$ and $n = 3$ for Xe and Kr within the resonance at 4 ML is visible. The only free parameter within the model that was adjusted in order to achieve good agreement for the binding energies is the dielectric constant of the adlayer. It was scaled for all three rare gases in the same way by $\epsilon_{calc} = 1 + 0.5(\epsilon - 1)$, with ϵ being the bulk dielectric constant ($\epsilon = 2.19$, 1.86, 1.70 for Xe, Kr, Ar[110]). This reduction leads to a decrease of the calculated binding energies as well as the lifetimes and roughly accounts for the screening properties at the two interfaces. The agreement for the lifetimes is, in particular, good for $n = 1$. Even the saturation of the $n = 1$ lifetime for Xe and Kr is well described, and the $n = 2$ resonance is generated at the correct position at 4 ML. However, the lifetimes of $n = 2$ and $n = 3$ partly lie more than a factor of 3 above the experimental values. This is probably an indication that the bulk penetration approximation is not as satisfied for high-n states on Xe and Kr as for the nonpenetrating $n = 1$ state as well as for the whole Rydberg series on the clean and Ar-covered surfaces.

In any case, the lifetime is the more sensitive quantity, since it depends on the exact form of the wave function and interaction in a small spatial region while the binding energy is a more global quantity which is sampled over a larger region, especially for higher quantum numbers. Such behavior can be found also for Rydberg states in atoms, where, for example, the hyperfine interaction which depends primarily on the probability density at the nucleus is much more sensitive to the composition of the wave function than the

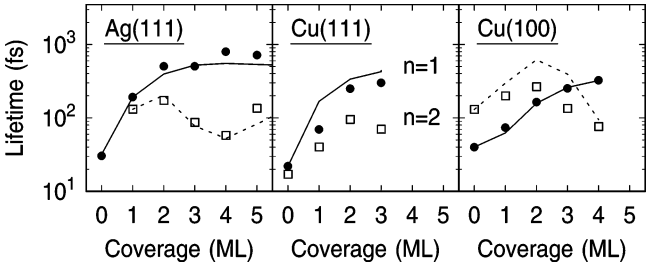

Figure 15. Coverage-dependent lifetimes of $n = 1$ and 2 for Xe adsorption on the noble-metal surfaces Ag(111) (ref 52), Cu(111) (ref 53), and Cu(100) (ref 57) along with computational results of the atomic model (lines). Lifetimes could not be computed for the $n = 2$ surface resonance on Cu(111). Reprinted Figure 11 from ref 57, copyright 2004, with kind permission of Springer Science and Business Media.

binding energy.[111] The enhanced sensitivity of the lifetimes to the exact form of the potential is also underlined by the fact that model calculations for Kr within the dielectric continuum model which neglects the atomic corrugation in the adlayer exhibit almost quantitative overall agreement but cannot reproduce the detailed coverage dependence.[112] In particular, the quantum-well resonance is placed at 2 ML of coverage instead of 4 ML, and the lifetime of $n = 1$ is predicted to decrease instead of saturate beyond 2 ML.

It has been shown that the atomic model can also be used for the simulation of other systems.[57] In Figure 15 the lifetime changes upon Xe adsorption are compared for the three different noble-metal surfaces Ag(111), Cu(111), and Cu(100). In all cases, very good agreement between experiment and theory is found, whereby the same value for the dielectric constant of Xe ($\epsilon = 1.65$) has been used. The (111) surfaces of Ag and Cu exhibit a qualitatively similar behavior. Differences between the (111) and (100) noble metal surfaces can be understood easily, because, for the former, the image-potential states lie close to the top of the band gap, where the penetration of the wave functions into the metal is high, while, for the latter, they are near the band gap center, where the bulk penetration is minimized. This leads for the (111) surfaces to a smaller lifetime of $n = 2$ in comparison to $n = 1$, as it is closer to the upper edge of the band gap. On Cu(111), the $n = 2$ state is even in resonance with the unoccupied metal band. Similarly, the steep initial rise of the $n = 1$ lifetime on the (111) surfaces is generated by the work function drop upon Xe adsorption that moves the image-potential states toward the center of the gap.[17]

The one-dimensional model potential gives a microscopic understanding of the influence of the electronic structure of

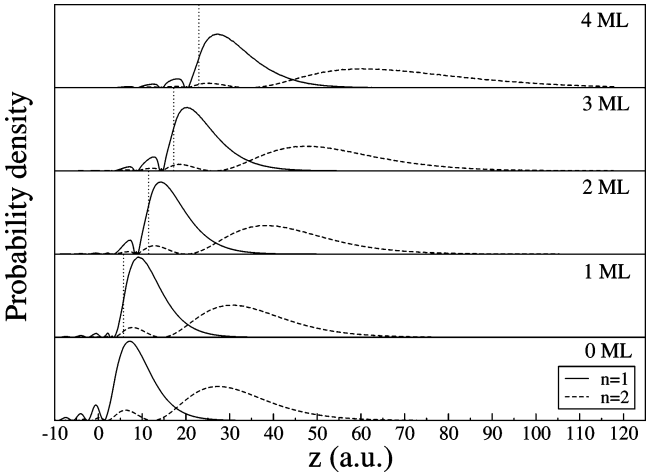

Figure 16. Calculated probability density for $n = 1$ (solid line) and $n = 2$ (dashed line) for 0−4 ML of Ar/Cu(100). The position of the last Ar plane is indicated with a dotted line. $z = 0$ corresponds to the metal jellium edge. Reprinted from ref 27, copyright 2003, with permission from Elsevier

the rare-gas layers. However, the calculation of the lifetimes is still based on the bulk penetration approximation. As shown by Echenique *et al.*,[10,45] there are sizable nonlocal contributions of the electron−electron interaction, which are not taken into account within the bulk penetration approximation. Only in favorable cases such as the clean Cu(001) surface[10] do the nonlocal contributions to the total decay rate cancel each other to a large extent. It is not clear a priori if this cancellation holds also for the rare-gas covered Cu(100) surface.

5.2. Many-Body Calculations

The description of the interaction between an electron and the rare-gas covered surface by a one-dimensional potential makes it possible to realize realistic many-body calculations as in the case of the clean surface. Machado *et al*. computed inelastic lifetimes for Ar/Cu(100) within the GW approximation of the many-body theory from the imaginary part of the self-energy.[94] This technique makes it possible to predict accurate lifetimes of image-potential states[10,46] and also of occupied surface states[113] in the case of clean metal surfaces (see also the paper by Chulkov et al.[114] in this issue). Ar/Cu(100) is the favorable system from a theoretical point of view, because it possesses the largest band gap, smallest polarizability, and weakest interaction both between the atoms and with the metal substrate. For this system, the same one-dimensional parametrized potential as for the calculations within the bulk penetration approximation presented above has been used for the description of the image-potential states. The probability density for $n = 1$ and $n = 2$ for 0−4 ML of Ar is shown in Figure 16, which clearly demonstrates the repulsion of the image-state electron due to the Ar layers for both states. To avoid the enormous computational effort of a true three-dimensional calculation,[7,115] the final states and the density response function of the metal/adsorbate system were approximated by those of the clean surface which can be described in a free-electron-like picture with translational invariance parallel to the surface. The error thus introduced is expected to be small, since the localized Ar levels lie quite deep in energy and are only weakly coupled to the Cu substrate. Thus, they do not provide additional decay channels compared to the case of the clean surface.

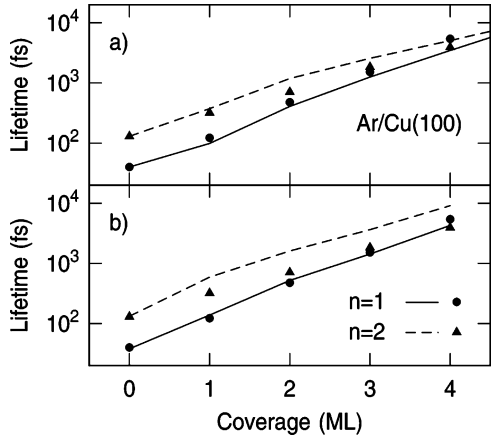

Figure 17. Theoretical lifetimes (lines) obtained from (a) the bulk penetration approximation (cf. also Figure 11) and (b) the many-body calculation in comparison with the experimental data (symbols). Compiled from refs 57 and 94.

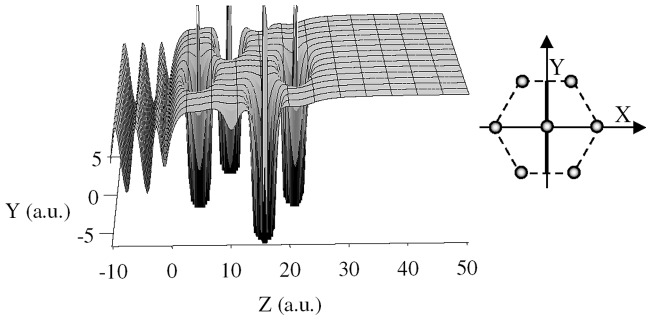

Figure 18. Two-dimensional cut of the 3d interaction potential between an electron and the Ar/Cu(100) system (4 ML coverage). The *z*-axis is perpendicular to the surface ($z > 0$ in a vacuum; the Cu image plane is at $z = 0$), and the *y*-axis is one of the axes parallel to the surface. The orientation of the *y*-axis with respect to the Ar hexagonal array is given in the inset. Reprinted from ref 120, copyright 2003, with permission from Elsevier

Figure 17b shows the experimental and calculated coverage dependence of the lifetimes. The agreement is particularly good for $n = 1$ compared to the calculations within the bulk penetration approximation. This results from the almost perfect cancellation of the nonlocal contributions, as for the clean surface. This cancellation is most probably fortuitous and will not occur in general if compared to other adsorbate systems and electronic states. The agreement is less perfect for $n = 2$, which may be a hint that a one-dimensional description cannot cover all details of the interaction.

5.3. 3D Potential

A truly three-dimensional approach for the description of the Ar/Cu(100) system was chosen by Marinica *et al.*[116,117] They computed a parameter-free three-dimensional potential for the interaction of the image-state electron with the Ar layer (see also the paper by Chulkov et al.[114] in this issue), which is depicted in Figure 18. The potential between the electron and the single atoms of the layer and the mutual polarization of the Ar atoms was considered, allowing a correct description of screening inside the layer. The electron−Ar potential was adjusted to electron-scattering data while the total three-dimensional potential was assumed to be the sum of the electron−Ar and the electron−metal interactions. The latter was included by a well-tested one-dimensional potential that has been applied with great success to many-body calculations of inelastic decay at metal

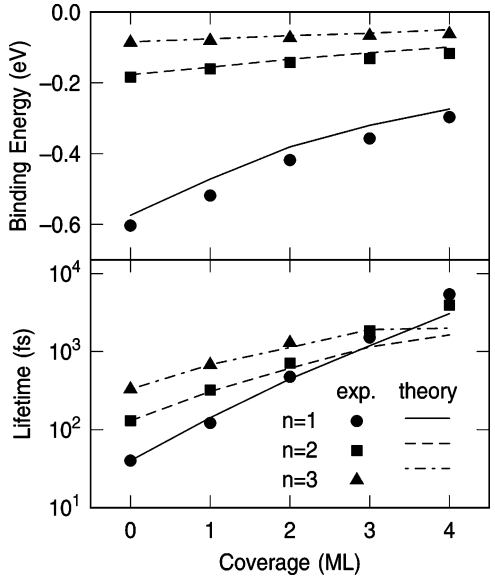

Figure 19. Binding energies and lifetimes of $n = 1-3$ for Ar/Cu(100) as a function of Ar coverage as calculated within the three-dimensional model (lines) together with the experimental data points. Reprinted (Figure 3) with permission from ref 116 (http://link.aps.org/abstract/PRL/v89/p046802). Copyright 2002 The American Physical Society.

surfaces.[45] Finally, the Schrödinger equation was solved by using a three-dimensional wave packet propagation method. The change of lifetimes upon Ar adsorption was estimated by the use of the bulk penetration approximation. As shown in Figure 19, the coverage dependence of the lifetimes computed with this three-dimensional model is very similar to the bulk-penetration and many-body results obtained by using the one-dimensional atomic model. Up to 2 ML, the three-dimensional model fits slightly better than the other two theories, in particular for $n = 2$ and $n = 3$, whereas at higher coverages the lifetimes appear to saturate. This saturation effect has been explained by the interplay between the increasing thickness of the repulsive layer and the decreasing binding energies, which lower the effective height of the barrier. Details of the electronic structure or image dipoles of the polarized layer may also be involved. In general, the three-dimensional calculation confirms the results of the one-dimensional theories. In fact, the three-dimensional wave functions presented in ref 116, when averaged in the surface plane, resemble those of the one-dimensional atomic model.

6. Buried Interface States

Most of the studies on adsorbate systems, which use 2PPE or conventional electron spectroscopy, remained restricted to films that were only a few monolayers thick. For image-potential states that are pushed away from the metal, this is caused by the reduced overlap with bulk states, which inhibits an efficient population by optical excitation with increasing layer thickness. For electronic states that are located at the metal/adsorbate interface, on the other hand, this restriction is generally governed by the limited escape depth of electrons in matter. The dynamics of electrons located at buried solid/solid interfaces, however, is not only of vast technological significance but also of great fundamental importance. Interesting issues are, for example, the elastic or quasi-elastic transfer of electrons across the boundary of two materials with different geometric and electronic structures and the dynamical many-body response of interface electrons leading to inelastic decay. Rohleder *et al*. could recently show for Ar/Cu(100) that the screened image-potential of the metal within the rare-gas adlayers supports a series of unoccupied electronic states located at the metal/rare-gas interface, which nevertheless can be accessed by 2PPE up to an Ar layer thickness of more than 20 nm.[31]

6.1. Origin

The origin of these interface states is the image-potential of the metal which is screened within the rare-gas layer. For a rare-gas crystal without the metal substrate, the conduction band in the direction perpendicular to the surface develops from a finite series of quantum-well states into the continuous delocalized band with increasing layer thickness. These states are derived from the unoccupied 6s (5s, 4s) level of the Xe (Kr, Ar) atoms. Adsorbed on a metal, the attractive image-potential of the metal within the rare-gas crystal represents a trap for electrons at the rare-gas/metal interface. In the limit of an adlayer of infinite thickness, an infinite Rydberg series below the conduction band minimum with energies

$$E_{n'} = E_{CBM} - \frac{0.85\ \text{eV}}{(n' + a)^2}\frac{m_{eff}}{\epsilon^2}, \quad n' = 1, 2, \ldots \qquad (11)$$

is formed. This is already evident from the form of the potential V_{in} within the dielectric continuum model (compare eq 4). Reduction of the adlayer thickness leads to an upshift of the interface-state energies such as in a simple quantum well. For an adlayer with negative electron affinity, such as Ar, the interface states are located above E_{vac} and can be observed also as final state resonances by conventional photoemission spectroscopy.[118] However, decay into the vacuum will be suppressed with increasing layer thickness since the screened image-potential forms a potential barrier on the vacuum side. The energetic location of the interface states above the vacuum level has most likely prevented an earlier experimental detection of these states because one usually avoids pump photon energies above the work function in 2PPE experiments in order to suppress the one-photon photoemission (1PPE) background.[69] This transition from a short-lived scattering resonance into a quasi-bound interface state could be followed by 2PPE.[31] Figure 20 shows as an example the probability density of the first member $n' = 1$ of the series of interface states in Ar/Cu(100), as can be calculated by solving the one-dimensional Schrödinger equation for positive energies using the same model potential as has been used for the description of the image-potential states (section 5.1). The probability density oscillates with the period of the rare-gas lattice as for a Bloch-type state, but its envelope has the form of a hydrogen-like image-potential state in front of the metal. The maximum of the probability density of the interface state is located further away from the metal/rare-gas interface compared to that of the $n = 1$ image-potential state on the clean surface due to the screening and the small effective mass within the Ar layer. Compared to the clean surface, this results in a larger lifetime for decay into the metal, which made it possible to study the dynamics of these interface states in detail as a function of film thickness and parallel momentum.

6.2. 2PPE Spectroscopy

Energy-resolved 2PPE spectra for Ar/Cu(100) show only the bound image-potential states below E_{vac} at low Ar

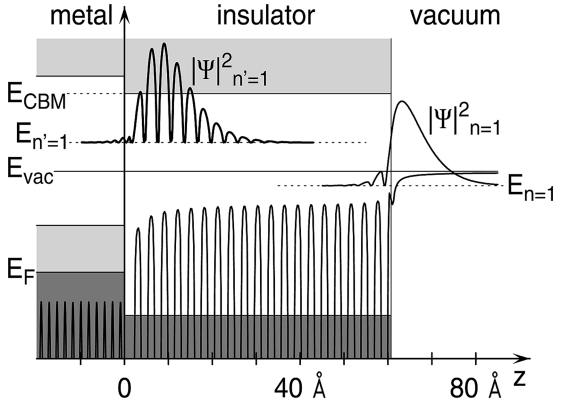

Figure 20. Schematic energy diagram of a 20 monolayer (ML) Ar film on Cu(100) indicating (from left to right) the pseudopotential of sp electrons in Cu, the screened corrugated potential of a single electron in Ar, and the vacuum image potential. Filled and empty electronic bands are marked by dark and light shades. $|\Psi|^2_{n=1}$ denotes the calculated probability density of the first image-potential state. $|\Psi|^2_{n'=1}$ is a further solution located at the Cu/Ar interface. Reprinted (Figure 1) with permission from ref 31 (http://link.aps.org/abstract/PRL/v94/p017401). Copyright 2005 The American Physical Society.

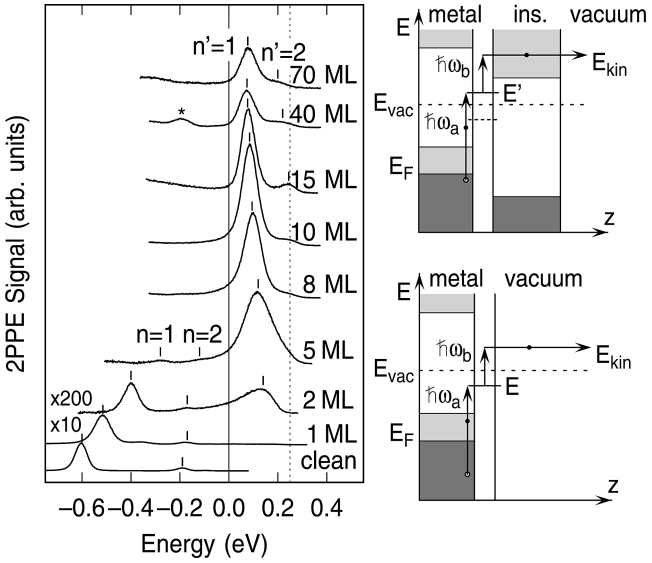

Figure 21. Energy-resolved 2PPE spectra for Ar layers of variable thickness showing the $n' = 1$ and 2 interface states and at low coverage also the $n = 1$ and 2 image-potential states. The asterisk denotes an Ar defect state induced by laser irradiation. The energies are referenced to the vacuum level that was obtained from the low-energy cutoff of the spectra, and the dotted vertical line marks the conduction band minimum of bulk Ar. The energy schemes on the right indicate the 2PPE process for surface states (bottom) and interface states (top) with electronic bands marked by shades. Reprinted (Figure 2) with permission from ref 31 (http://link.aps.org/abstract/PRL/v94/p017401). Copyright 2005 The American Physical Society.

coverage (Figure 21). With increasing coverage, their binding energies relative to E_{vac} decrease, and their intensity drops rapidly due to the repulsion from the Cu interface, which decreases the overlap with the Cu bulk electrons and therewith the excitation probability. Starting at 2 ML, the $n' = 1$ interface state becomes visible as a broad feature above the vacuum energy that grows in intensity, shifts down in energy, and narrows in line width when the coverage is further increased. The energy and intensity of this peak stay constant at a high coverage above 15 ML. For coverages larger than 10 ML, also the $n' = 2$ state can be assigned,

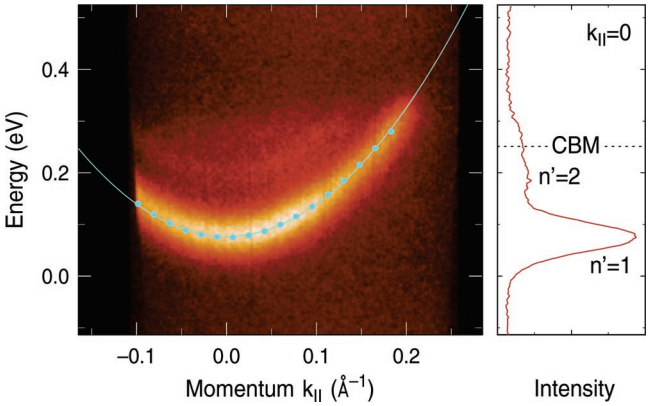

Figure 22. (left) $E(k_{||})$ 12PPE spectrum for 25 ML of Ar/Cu(100) acquired with a display-style electron analyzer. The solid line depicts the parabolic dispersion of the $n' = 1$ interface state. The dots mark the points used for evaluation of the time-resolved pump−probe traces. (right) 2PPE energy spectrum for $k_{||} = 0$ obtained from a cut through the 2d spectrum with a width of about 0.018 Å^{-1}. The dashed line shows the position of the conduction band minimum of Ar. Reprinted with permission from ref 109. Copyright 2005 IOP Publishing Ltd. and Deutsche Physikalische Gesellschaft.

which exhibits a similar behavior. In the limit of very thick layers, the states converge to energies that lie slightly below the conduction band minimum of Ar.

Figure 22 shows 2PPE data of the interface states in a 25 ML Ar film obtained with a display-style electron analyzer which makes it possible to determine the dispersion $E(k_{||})$ in a single measurement.[109] The parabolic dispersion of the n' $= 1$ state and even that of the $n' = 2$ state can be clearly resolved. Their effective mass has been determined to be $m_{eff} = 0.61 \pm 0.1$,[109] while the effective mass of the $n = 1$ image-potential state of clean Cu(100) is close to one.[119] The lower effective mass of the interface states reflects their confinement within the Ar adlayer. It agrees with recent theoretical work on these resonance states in very thin Ar films[120] using the 3D model described in section 5.3 and is very close to the effective mass at the conduction band minimum of Ar, where an effective mass of 0.53 ± 0.01 has been measured using low-energy electron-transmission spectroscopy.[121]

The feasibility of 2PPE spectroscopy of electronic states which are deeply buried under an insulating layer can be understood as follows: In a usual surface 2PPE experiment, the probe photon lifts the electrons from the intermediate state, for example, an image-potential state, directly into unbound vacuum states (Figure 21, bottom right). In the case of the interface states $n' = 1$, 2, the probe pulse promotes the electrons into the Ar conduction band (Figure 21, top right), from which they escape to the vacuum by ballistic transport through the layer. The spectroscopic results indicate that this transport occurs without appreciable loss of energy or momentum for layer thicknesses up to roughly 100 Å. Sharp peaks and an almost constant maximum count rate of 5000/s can be observed. For thicker Ar layers, however, the count rate decreases and peak broadening is noticeable (spectra for 40 and 70 ML in Figure 21). Contrasting the 2PPE process, the use of a pump photon energy well above the work function of Ar/Cu(100) did not pose a serious limitation in the present measurements because the one-photon background was efficiently blocked by the insulating layer.

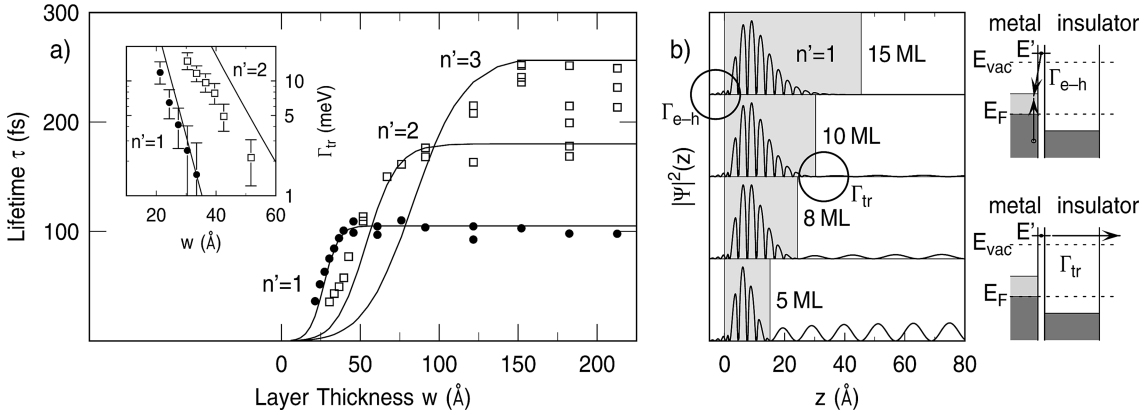

Figure 23. (a) Summary of the experimental lifetimes (symbols) as a function of Ar layer thickness (1 ML $\hat{=}$ 3.04 Å). Simulated curves were calculated as $\tau = (\Gamma_{tr}/\hbar + 1/\tau_{sat})^{-1}$ from the theoretical rates of elastic transfer Γ_{tr} and the experimental high-coverage lifetimes τ_{sat}. Inset: elastic rates Γ_{tr}. (b) Computed probability densities of the $n' = 1$ state for different Ar coverages. Reprinted (Figure 4) with permission from ref 31 (http://link.aps.org/abstract/PRL/v94/p017401). Copyright 2005 The American Physical Society.

6.3. Tunneling and Inelastic Decay

Time-resolved measurements of the interface states $n' = 1$ and $n' = 2$ revealed a strong dependence of the lifetimes on the adsorbed layer thickness, as summarized in Figure 23a. The lifetime τ of the $n' = 1$ state is 40 fs at 8 ML, while above 15 ML it saturates at 100 fs. The lifetime of the $n' = 2$ state lies below that of the $n' = 1$ state for thinner layers, but it approaches a value near 200 fs above 30 ML. The data for the $n' = 2$ state show a larger scatter at high coverages due to contributions of energetically close-lying and long-living states with $n' \geq 3$, which are experimentally difficult to separate. The curves separate in two regions: at low coverage, that is, below 15 ML for $n' = 1$ and 30 ML for $n' = 2$, there is a strong rise of the lifetimes with increasing layer thickness, while at high coverage the lifetimes of both states approach constant values of 100 fs and around 200 fs, respectively. This behavior stems from two different decay processes of the interface electrons, which are sketched in the inset of Figure 23b). The strong variation of the lifetimes in the low-coverage regime arises from resonant electron transfer through the insulating overlayer. It can be looked at as a leakage of the wave function, that is confined to a thin layer, into the vacuum. This *elastic* decay channel can exist, because the energies of the interface states lie above the vacuum level. Thus, the interface states are, in principle, not bound to the surface but form short-lived resonances in the case of thin layers. However, when the layer thickness becomes larger than the spatial spread of the wave function, which is localized at the interface due to image forces, this decay path becomes weaker and finally vanishes, because then the wave function is contained completely inside the layer (Figure 23b). Under this condition, only the second, inelastic decay process survives. The corresponding decay rate Γ_{e-h} can be determined from the experimental high-coverage lifetimes τ_{sat} by $\Gamma_{e-h} = \hbar/\tau_{sat}$. As in the case of image-potential states, it originates from *inelastic* scattering with the electrons of the metal and scales with the bulk penetration of the wave function of the interface state. Although the bulk penetration and dielectric screening may be slightly affected by the film thickness, this decay channel can be regarded as approximately constant. Thus, the elastic transfer rate Γ_{tr} is given by $\Gamma_{tr} = \hbar/\tau - \hbar/\tau_{sat}$. As shown in the inset of Figure 23a, Γ_{tr} decreases exponentially with layer thickness, as for tunneling through a square barrier, even if the screened image-potential decreases more gradually.

Angle- and time-resolved 2PPE experiments on 25-ML thick Ar films on Cu(100) revealed a momentum dependence of the inelastic decay rate of the $n' = 1$ interface state.[109] At this coverage the $n' = 1$ interface state is completely confined to the Ar layers, and elastic decay due to tunneling can be neglected. Figure 22 shows typical raw data for a fixed delay of 67 fs between pump and probe pulses. The dynamics of the inelastic decay along the dispersion curve has been determined by recording such images as a function of pump−probe delay. For the clean Cu(100) surface, it has been shown that the momentum dependence of the inelastic decay rate is governed by inter- and intraband decay processes, both driven by electron−electron interaction.[21] The momentum dependence of the interband decay results from the energy and momentum dependence of the electron−electron interaction as well as from a $k_{||}$ dependence of the image-state wave function due to the dispersion of the bulk bands. The intraband decay within the bands of the image-states has a comparable magnitude due to the almost complete spatial overlap of image-potential wave function for different $k_{||}$. As shown in Figure 24, the smaller rate for inelastic decay of the $n' = 1$ interface state at the $\bar{\Gamma}$-point ($k_{||} = 0$) goes along with a weaker dependence on $k_{||}$ if compared with the $n = 1$ state on the clean surface. A similar relation has been found for the momentum-dependent decay rate of the image-potential states on mono- and bilayers of Xe on Ag(111).[59] There, the bilayer exhibits a weaker dependence on $k_{||}$ as well as a smaller decay rate at the band bottom compared to the monolayer. This can be simply understood if the momentum-dependent relaxation dynamics of the $n' = 1$ state is governed by the same scattering processes as for the $n = 1$ state on the clean surface. Then both the decay rate and its momentum dependence should scale with the same factor compared to the case of the $n = 1$ state, as confirmed by the dashed line in Figure 24. This empirical factor of 2.75 should be related to the different penetrations of the $n' = 1$ and $n = 1$ wave functions into the Cu bulk if nonlocal contributions of the electron−electron interaction cancel each other to the same extent as they do for the image-potential states.[94] However, the ratio of the calculated bulk penetrations is 4.7. This indicates either that the local description by the bulk penetration argument could be not appropriate for the interface states or that the 3D corrugation of the wave

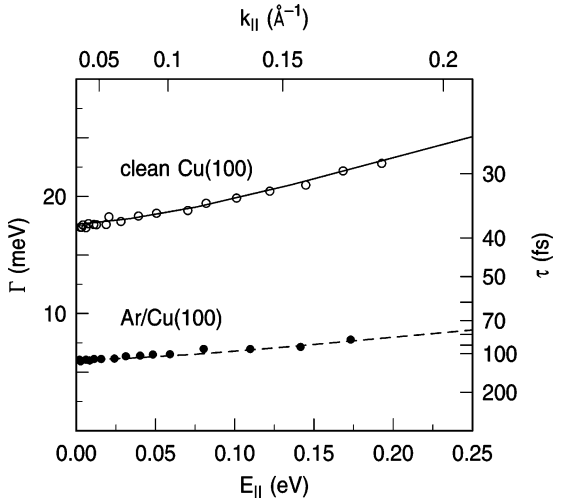

Figure 24. Decay rates of the first image-potential state (open symbols) and the first Ar interface state (closed symbols) on Cu(100) as a function of the kinetic energy of parallel motion $E_{||} = \hbar^2 k_{||}^2/2m_{eff}m_0$. The solid curve indicates the theoretical values for the clean surface from ref 21. The dashed curve represents the same curve but scaled by a constant factor which has been obtained from the ratio of the lifetimes for the clean and Ar covered surfaces at $k_{||} = 0$. Reprinted with permission from ref 109. Copyright 2005 IOP Publishing Ltd. and Deutsche Physikalische Gesellschaft.

function in the Ar layer, which leads to a lateral variation of the coupling to the surface, could be crucial for the quantitative description of the decay. Decay processes mediated by phonons in the Ar layer as proposed for the system N_2/Xe/Cu(111)[96] should lead to a stronger $k_{||}$ dependence. However, scattering at defects is expected not to depend much on $k_{||}$,[24] which could contribute to a constant offset of the experimental decay rate compared to the scaled theoretical results. On the other hand, the inelastic decay rate of the $n' = 1$ state is very reproducible, as can be seen in Figure 23, in particular for layer thicknesses between 50 and 210 Å, which makes defect scattering due to imperfections of the Ar layer not very likely.

7. Organic Adlayers

During the last few years, the electron dynamics at the interface between organic molecules and metals has attracted much attention, partly due to its relevance for molecular-based electronics.[2] It has been reviewed in a number of recent papers by Zhu[2,26,122] and Harris and co-workers.[25,60,123] Thus, we will not discuss all aspects of this topic here, and we will concentrate on the main differences and similarities compared to image-potential states on rare-gas layers.

In the energy region which is probed by 2PPE, that is, mainly between E_F and E_{vac}, the electronic structure of rare-gas crystals is dominated by a delocalized conduction band. The localized valence band is separated by a large band gap, and direct excitations within the rare-gas layer play no role at optical frequencies. Instead of valence and conduction bands, the electronic structure of molecular adsorbates is usually classified by molecular orbitals such as the highest occupied molecular orbital (HOMO) and the lowest unoccupied molecular orbital (LUMO), both of which may be partly hybridized with electronic states of the metal. For molecular crystals, however, these levels form energy bands which reflect the translational periodicity of the adlayer, but these bands may be narrow, like a molecular resonance, if the electronic coupling between the molecules is weak. Examples for the observation of molecular resonances by 2PPE are CO,[80,97,124−126] Cs,[76,99,127−133] atomic oxygen,[98] molecular oxygen,[95] and benzene,[134−138] all adsorbed on Cu(111). In most 2PPE experiments, the initially unoccupied resonances are populated by excitation of metal electrons. For organic molecules, however, the energetic distance between the HOMO and LUMO level may be small enough for optical excitations within the adsorbate layer.[139]

In any case, the image-potential of the metal will be always superimposed on the molecular potential, and image-potential states may dominate the electronic structure around E_{vac}, in particular if the electronic coupling between the molecular orbitals and the metal is weak. Examples for the dominance of the image-potential states are alkanes/Ag(111),[56] benzene/Ag(111),[140] and naphthalene and anthracene on Ag(111).[66] As for rare-gas films, the binding energies and lifetimes of the image-potential states on these organic layers depend sensitively on the energetic position of the affinity level. Naphthalene and anthracene, however, have two attractive affinity levels, that is, two close lying bound conduction bands. Such an electronic structure cannot be described by the dielectric continuum model, in which the adsorbate layer is represented by a single affinity level and its dielectric constant. The qualitative arguments, however, are the same as those for layers with a single conduction band. For naphthalene, the $n = 1$ image-potential state is degenerated with the first conduction band. This results in a penetration of the electron into the layer, and a $n = 1$ lifetime of not more than 60 fs even for a trilayer has been observed. For anthracene, the $n = 1$ state is located in the gap between the two conduction bands and the adlayer forms a tunnel barrier. Thus, the lifetime is much longer and reaches 1.1 ps for the bilayer.[66]

Self-assembled monolayers of thiolates, which chemisorb on metal surfaces via a sulfur anchor, represent a case in which the 2PPE spectra are dominated by molecular resonances, and no image-potential states were observed for methanethiolate (CH_3S) on Ag(111)[139] and pentafluorothiophenolate (C_6F_5S) on Cu(111).[141]

In contrast to C_6F_5S, C_6F_6 binds only weakly to metal surfaces, with the first layer lying flat on the surface. Nevertheless, electron transfer by direct excitation of metal electrons into the LUMO at 2.9 eV above the Fermi level has been observed by 2PPE on C_6F_6/Cu(111).[142] The strong electronic coupling of this state to the metal surface is also reflected by its short lifetime of only 7 fs at 1 ML coverage.[143] With increasing coverage, the lifetime of the LUMO increases and the effective mass parallel to the surface decreases toward the mass of the free electron. This has been explained by an increasing delocalization in the direction perpendicular as well as parallel to the surface due to band formation caused by intramolecular interaction. Recent time- and angle-resolved experiments with improved time-resolution revealed a delayed build up of the LUMO population at $k_{||} = 0$, which has been attributed to intraband scattering within the delocalized band toward the band minimum.[144]

In addition to the electronic polarization of the metal and the adlayer, an excess electron can also induce a rearrangement of the adsorbate atoms by intra- or intermolecular polarization. This can lead to a dynamical localization of the electron due to self-trapping into a small or large polaron, respectively. Such a localization mechanism has been observed for image-potential states on alkane layers. These

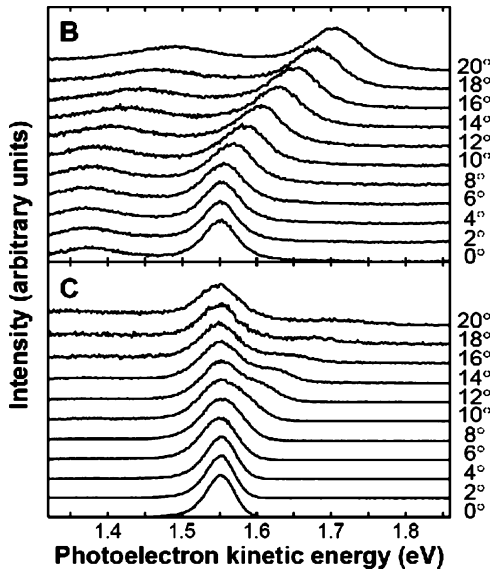

Figure 25. Angle-resolved 2PPE spectra of the $n = 1$ image-potential state for a bilayer of *n*-heptane/Ag(111) taken at pump−probe delay times of 0 (B) and 1670 fs (C). Initially, the electron is delocalized and the $n = 1$ state shows a strong dispersion. The collapse into a nondispersive localized state occurs within a few hundred femtoseconds. Reprinted with permission from *Science* (http://www.aaas.org), ref 28. Copyright 1998 American Association of the Advancement of Science.

σ-bonded hydrocarbons have a negative electron affinity similar to that of Ar, which leads to a strong decoupling of the image-potential states, as has been shown by time-resolved 2PPE at $k_{||} = 0$.[51,145] In contrast to the case of rare-gas layers, however, angle-resolved 2PPE spectroscopy has revealed that the image-potential states on bilayers and trilayers of *n*-alkanes show, apart from a delocalized ($m_{eff} \approx 1$), also a localized ($m_{eff} \approx \infty$) component.[56] The nondispersive peak has been observed for different chain alkanes such as *n*-pentane, as well as for the ring alkane cyclohexane, but not for neopentane.[146] It has been assigned to an excess electron which collapses from the delocalized image-potential state into a localized two-dimensional small polaron by creating itself a potential well in the alkane layer due to polarization and displacement of the atoms surrounding it. Ge *et al*. have demonstrated that the unique capabilities of time-resolved 2PPE can be used to investigate the dynamics of this self-trapping localization process directly in the time domain.[28,147] They observed the transition from a well-defined, delocalized image-potential state into a localized state within a few hundred femtoseconds, as shown in Figure 25. A dependence of the localization time on parallel momentum and temperature has been found, which could be explained by an activated polaron formation model. So far, this is the only example in which polaron formation has been observed at adsorbate/metal interfaces.

For polar molecules, dynamical localization of an excess electron can occur due to a reorientation of the molecular dipoles, that is, by the process of solvation. This has been observed by time-resolved 2PPE for the polar organic molecules acetonitrile, butyronitrile, and alcohol on Ag(111) in the group of Harris.[29,148,149] In these experiments, the excess electron was excited in an image-potential state. Wolf and co-workers investigated in detail the trapping of electrons at metal/ice interfaces where the excess electron was excited from the metal into the conduction band of the ice layers. The dependence of the ultrafast dynamics on molecular and

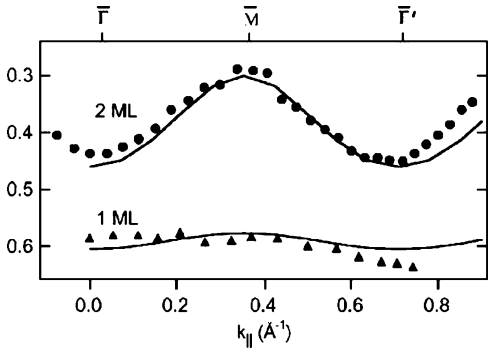

Figure 26. Dispersion of the $n = 1$ image-potential state parallel to the surface on Cu(111) covered with 1 or 2 ML of C_{60}. Filled symbols are experimental results; solid curves are from quantum mechanical simulations.[156] Reprinted with permission from ref 122. Copyright 2004 American Chemical Society.

electronic structure has been systematically studied by investigating amorphous D_2O and H_2O on Cu(111) and amorphous and crystalline D_2O/Ru(0001).[30,150−154]

A strong corrugation of the electrostatic potential in the adlayer can result in a large effective electron mass, which would represent some sort of static localization. Such an effect has been observed for C_{60},[155,156] which grows epitaxially on Cu(111). Due to the strong charge transfer from the metal to the first monolayer, C_{60} films form a lattice of dipoles at the interface with translational periodicity. This results in a large effective mass of the image-potential states, and almost no dispersion has been observed for 1 ML coverage (Figure 26). For a coverage of 2 ML C_{60}, the $n = 1$ state shows a strong dispersion with an effective mass of $m_{eff} = 3$, since the electron is located further away from the interface, where it samples a smoother potential. For a periodic potential, however, the electron wave function is not localized to a single molecule. The latter type of static localization can occur in disordered films, as has been shown for multilayers of benzene.[140]

8. Conclusion

Image-potential states on rare-gas covered metal surfaces has been proven to be an ideal model system for the study of electron dynamics at metal/insulator interfaces using two-photon photoemission. The extensive experimental work has shown that their binding energies and lifetimes for inelastic decay are most essentially governed by the electron affinity and the dielectric constant of the rare-gas layer. Even relatively simple theoretical models which describe the rare-gas layer as a homogeneous dielectric achieve qualitative agreement with the experimental data, in particular for rare-gas layers with negative electron affinity. The quantum-well character of image-potential states which penetrate into layers with positive electron affinity, however, can be correctly reproduced only by models which take into account not only the image-potential within the layer but also the periodic crystal potential which forms the electronic bands of the rare-gas solid. The one-dimensional character of image-potential states made it even possible to perform realistic many-body calculations of the quasi-particle dynamics, which cover the nonlocal character of the interaction between an electron in an image-potential state and the electronic system of the metal. The role of the three-dimensional corrugation of the electron potential within the rare-gas layers has been accessed, which will need further attention, in particular for

image-potential states which penetrate into the rare-gas layers.

New electronic states have been found for thick Ar films on Cu(100). These states are similar to image-potential states but spatially located at the metal/rare-gas interface and bound relative to the rare-gas conduction band minimum. Despite the fact that these interface states are buried under Ar films as thick as 200 Å, their dynamics could be studied by time-, energy-, and angle-resolved 2PPE. Two distinct decay channels have been separated: (1) inelastic decay by e−h excitation in the metal and (2) elastic transfer through the Ar layer. The latter is a consequence of the negative electron affinity of Ar, which results in an energetic location of the interface states above the vacuum level. This decay channel is strongly suppressed if the layer thickness becomes larger than the spatial extent of the interface-state wave function. Thus, the inelastic decay could be studied in detail for thick films. The existence of such buried image-potential states makes it possible to investigate electron transfer and decay processes, which are of general relevance to metal/insulator interfaces, in a simple and well-defined model system.

The studies on molecular layers have shown that image-potential states persist on a variety of physisorbed layers, in particular, for adlayers with negative electron affinity. These show the same decoupling of the image-potential states as that for the rare-gas Ar. For molecular adlayers with positive electron affinity, however, the affinity level may be strongly coupled with the metal or with the image-potential states. Thus, the electron transfer is fast and dominated by the affinity level. In addition, molecular adlayers have shown a variety of localization phenomena which are not present in rare-gas layers.

9. Acknowledgment

We thank E. V. Chulkov, K. Duncker, P. M. Echenique, P. Feulner, J.-P. Gauyacq, K.-L. Kompa, M. Machado, D. C. Marinica, F. Rebentrost, and M. Rohleder for a fruitful and pleasant collaboration on this work. Support by the Deutsche Forschungsgemeinschaft through HO 2295/1, the Max-Planck Society, and the Center for Optodynamics Marburg is gratefully acknowledged.

10. References

(1) Schroder, D. K. *Semiconductor Material and Device Characterization*; John Wiley & Sons: New York, 1998.
(2) Zhu, X. Y. *Surf. Sci. Rep.* **2004**, *56*, 1.
(3) Menzel, D. *Nucl. Instrum. Methods Phys. Res., Sect. B: Beam Interact. Mater. At.* **1995**, *101*, 1.
(4) Dai, H. L., Ho, W., Eds. *Laser Spectroscopy and Photochemistry on Metal Surfaces*; World Scientific: Singapore, 1995.
(5) Tanimura, K., Ueba, H., Eds. *Proceedings of the Tenth International Workshop on Desorption Induced by Electronic Transitions (DIET-10)*; *Surf. Sci.* **2005**, *593*, 1−336.
(6) Nienhaus, H. *Surf. Sci. Rep.* **2002**, *45*, 3.
(7) Echenique, P. M.; Berndt, R.; Chulkov, E. V.; Fauster, T.; Goldmann, A.; Höfer, U. *Surf. Sci. Rep.* **2004**, *52*, 219.
(8) Höfer, U.; Shumay, I. L.; Reuss, C.; Thomann, U.; Wallauer, W.; Fauster, T. *Science* **1997**, *277*, 1480.
(9) Shumay, I. L.; Höfer, U.; Thomann, U.; Reuss, C.; Wallauer, W.; Fauster, T. *Phys. Rev. B* **1998**, *58*, 13974.
(10) Chulkov, E. V.; Sarría, I.; Silkin, V. M.; Pitarke, J. M.; Echenique, P. M. *Phys. Rev. Lett.* **1998**, *80*, 4947.
(11) Reuss, C.; Shumay, I. L.; Thomann, U.; Kutschera, M.; Weinelt, M.; Fauster, T.; Höfer, U. *Phys. Rev. Lett.* **1999**, *82*, 153.
(12) Weinelt, M.; Reuss, C.; Kutschera, M.; Thomann, U.; Shumay, I. L.; Fauster, T.; Höfer, U.; Theilmann, F.; Goldmann, A. *Appl. Phys. B* **1999**, *68*, 377.
(13) Sarría, I.; Osma, J.; Chulkov, E. V.; Pitarke, J. M.; Echenique, P. M. *Phys. Rev. B* **1999**, *60*, 11795.
(14) Schäfer, A.; Shumay, I. L.; Wiets, M.; Weinelt, M.; Fauster, T.; Chulkov, E. V.; Silkin, V. M.; Echenique, P. M. *Phys. Rev. B* **2000**, *61*, 13159.
(15) Link, S.; Dürr, H. A.; Bihlmayer, G.; Blügel, S.; Eberhardt, W.; Chulkov, E. V.; Silkin, V. M.; Echenique, P. M. *Phys. Rev. B* **2001**, *63*, 115420.
(16) Klamroth, T.; Saalfrank, P.; Höfer, U. *Phys. Rev. B* **2001**, *64*, 035420.
(17) Wolf, M.; Knoesel, E.; Hertel, T. *Phys. Rev. B* **1996**, *54*, R5295.
(18) Knoesel, E.; Hotzel, A.; Wolf, M. *J. Electron Spectrosc. Relat. Phenom.* **1998**, *88*, 577.
(19) Berthold, W.; Güdde, J.; Feulner, P.; Höfer, U. *Appl. Phys. B* **2001**, *73*, 865.
(20) Shen, X. J.; Kwak, H.; Radojevic, A. M.; Smadici, S.; Mocuta, D.; Osgood, R. M. *Chem. Phys. Lett.* **2002**, *351*, 1.
(21) Berthold, W.; Höfer, U.; Feulner, P.; Chulkov, E. V.; Silkin, V. M.; Echenique, P. M. *Phys. Rev. Lett.* **2002**, *88*, 056805.
(22) Roth, M.; Pickel, M. T.; Wang, J. X.; Weinelt, M.; Fauster, T. *Phys. Rev. Lett.* **2002**, *88*, 096802.
(23) Weinelt, M. *J. Phys.: Condens. Matter* **2002**, *14*, R1099.
(24) Boger, K.; Weinelt, M.; Fauster, T. *Phys. Rev. Lett.* **2004**, *92*, 126803.
(25) Harris, C. B.; Ge, N. H.; Lingle, R. L.; McNeill, J. D.; Wong, C. M. *Annu. Rev. Phys. Chem.* **1997**, *48*, 711.
(26) Zhu, X. Y. *Annu. Rev. Phys. Chem.* **2002**, *53*, 221.
(27) Machado, M.; Chulkov, E. V.; Silkin, V. M.; Höfer, U.; Echenique, P. M. *Prog. Surf. Sci.* **2003**, *74*, 219.
(28) Ge, N. H.; Wong, C. M.; Lingle, R. L.; McNeill, J. D.; Gaffney, K. J.; Harris, C. B. *Science* **1998**, *279*, 202.
(29) Miller, A. D.; Bezel, I.; Gaffney, K. J.; Garrett-Roe, S.; Liu, S. H.; Szymanski, P.; Harris, C. B. *Science* **2002**, *297*, 1163.
(30) Gahl, C.; Bovensiepen, U.; Frischkorn, C.; Wolf, M. *Phys. Rev. Lett.* **2002**, *89*, 107402.
(31) Rohleder, M.; Berthold, W.; Güdde, J.; Höfer, U. *Phys. Rev. Lett.* **2005**, *94*, 017401.
(32) Berthold, W.; Feulner, P.; Höfer, U. *Chem. Phys. Lett.* **2002**, *358*, 502.
(33) Föhlisch, A.; Feulner, P.; Hennies, F.; Fink, A.; Menzel, D.; Sanchez-Portal, D.; Echenique, P. M.; Wurth, W. *Nature* **2005**, *436*, 373.
(34) Cole, E. M.; Cohen, H. M. *Phys. Rev. Lett.* **1969**, *23*, 1238.
(35) Shikin, V. B. *Sov. Phys. JETP* **1970**, *31*, 936.
(36) Grimes, C. C.; Brown, T. R. *Phys. Rev. Lett.* **1974**, *32*, 280.
(37) Echenique, P. M.; Pendry, J. B. *J. Phys. C: Solid State Phys.* **1978**, *11*, 2065.
(38) Echenique, P. M.; Pendry, J. B. *Prog. Surf. Sci.* **1989**, *32*, 111.
(39) Straub, D.; Himpsel, F. J. *Phys. Rev. Lett.* **1984**, *52*, 1922.
(40) Dose, V.; Altmann, W.; Goldmann, A.; Kolac, U.; Rogozik, J. *Phys. Rev. Lett.* **1984**, *52*, 1919.
(41) Giesen, K.; Hage, F.; Himpsel, F. J.; Riess, H. J.; Steinmann, W. *Phys. Rev. Lett.* **1985**, *55*, 300.
(42) Fauster, T.; Steinmann, W. Photonic Probes of Surfaces. In *Electromagnetic Waves: Recent Developments in Research*; Halevi, P., Ed.; North-Holland: Amsterdam, 1995; Vol. 2.
(43) Rhie, H. S.; Link, S.; Dürr, H. A.; Eberhardt, W.; Smith, N. V. *Phys. Rev. B* **2003**, *68*, 033410.
(44) Echenique, P. M.; Osma, J.; Silkin, V. M.; Chulkov, E. V.; Pitarke, J. M. *Appl. Phys. A: Mater. Sci. Process.* **2000**, *71*, 503.
(45) Echenique, P. M.; Pitarke, J. M.; Chulkov, E. V.; Rubio, A. *Chem. Phys.* **2000**, *251*, 1.
(46) García-Lekue, A.; Pitarke, J. M.; Chulkov, E. V.; Liebsch, A.; Echenique, P. M. *Phys. Rev. Lett.* **2002**, *89*, 096401.
(47) Lopez-Bastidas, C.; Maytorena, J. A.; Liebsch, A. *Phys. Rev. B* **2002**, *65*, 035417.
(48) Chulkov, E. V.; Silkin, V. M.; Echenique, P. M. *Surf. Sci.* **1999**, *437*, 330.
(49) Osma, J.; Sarria, I.; Chulkov, E. V.; Pitarke, J. M.; Echenique, P. M. *Phys. Rev. B* **1999**, *59*, 10591.
(50) Schoenlein, R. W.; Fujimoto, J. G.; Eesley, G. L.; Capehart, T. W. *Phys. Rev. B* **1991**, *43*, 4688.
(51) Lingle, R. L.; Ge, N. H.; Jordan, R. E.; McNeill, J. D.; Harris, C. B. *Chem. Phys.* **1996**, *205*, 191.
(52) McNeill, J. D.; Lingle, R. L.; Ge, N. H.; Wong, C. M.; Jordan, R. E.; Harris, C. B. *Phys. Rev. Lett.* **1997**, *79*, 4645.
(53) Hotzel, A.; Moos, G.; Ishioka, K.; Wolf, M.; Ertl, G. *Appl. Phys. B* **1999**, *68*, 615.
(54) Link, S.; Sievers, J.; Dürr, H. A.; Eberhardt, W. *J. Electron Spectrosc. Relat. Phenom.* **2001**, *114*, 351.
(55) Link, S.; Dürr, H. A.; Eberhardt, W. *Appl. Phys. A: Mater. Sci. Process.* **2000**, *71*, 525.
(56) Padowitz, D. F.; Merry, W. R.; Jordan, R. E.; Harris, C. B. *Phys. Rev. Lett.* **1992**, *69*, 3583.
(57) Berthold, W.; Höfer, U.; Feulner, P. *Appl. Phys. A* **2004**, *78*, 131.
(58) Harris, C. B.; McNeill, J. D.; Ge, N. H.; Jordan, R. E.; Lingle, R. L.; Wong, C. M. Femtosecond Studies of Electron Dynamics in Two-

Dimensions. In *Ultrafast Phenomena*; Barbara, P. F., Ed.; Springer-Verlag: Berlin, 1996.
(59) Wong, C. M.; McNeill, J. D.; Gaffney, K. J.; Ge, N. H.; Miller, A. D.; Liu, S. H.; Harris, C. B. *J. Phys. Chem. B* **1999**, *103*, 282.
(60) Ge, N. H.; Wong, C. M.; Harris, C. B. *Acct. Chem. Res.* **2000**, *33*, 111.
(61) Berthold, W.; Shumay, I. L.; Feulner, P.; Höfer, U. Effect of Xe adlayers on the lifetime of the image-potential states of Ru(0001). In *Ultrafast Phenomena XI*; Elsaesser, T., Fujimoto, J. G., Wiersma, D. A., Zinth, W., Eds.; Springer-Verlag: Berlin, 1998.
(62) Berthold, W.; Höfer, U.; Feulner, P.; Menzel, D. *Chem. Phys.* **2000**, *251*, 123.
(63) Cole, M. W. *Phys. Rev. B* **1971**, *3*, 4418.
(64) McNeill, J. D.; Lingle, R. L.; Jordan, R. E.; Padowitz, D. F.; Harris, C. B. *J. Chem. Phys.* **1996**, *105*, 3883.
(65) Chiang, T. C.; Kaindl, G.; Mandel, T. *Phys. Rev. B* **1986**, *33*, 695.
(66) Gaffney, K. J.; Miller, A. D.; Liu, S. H.; Harris, C. B. *J. Phys. Chem. B* **2001**, *105*, 9031.
(67) Bokor, J. *Science* **1989**, *246*, 1130.
(68) Rowe, M. W.; Liu, H. L.; Williams, G. P.; Williams, R. T. *Phys. Rev. B* **1993**, *47*, 2048.
(69) Haight, R. *Surf. Sci. Rep.* **1995**, *21*, 277.
(70) Schoenlein, R. W.; Fujimoto, J. G.; Eesley, G. L.; Capehart, T. W. *Phys. Rev. Lett.* **1988**, *61*, 2596.
(71) Schmuttenmaer, C. A.; Aeschlimann, M.; Elsayedali, H. E.; Miller, R. J. D.; Mantell, D. A.; Cao, J.; Gao, Y. *Phys. Rev. B* **1994**, *50*, 8957.
(72) Hertel, T.; Knoesel, E.; Wolf, M.; Ertl, G. *Phys. Rev. Lett.* **1996**, *76*, 535.
(73) Wolf, M. *Surf. Sci.* **1997**, *377*, 343.
(74) Petek, H.; Ogawa, S. *Prog. Surf. Sci.* **1997**, *56*, 239.
(75) Aeschlimann, M.; Bauer, M.; Pawlik, S.; Weber, W.; Burgermeister, R.; Oberli, D.; Siegmann, H. C. *Phys. Rev. Lett.* **1997**, *79*, 5158.
(76) Petek, H.; Weida, M. J.; Nagano, H.; Ogawa, S. *Science* **2000**, *288*, 1402.
(77) Höfer, U. *Appl. Phys. B* **1999**, *68*, 383.
(78) Blum, K. *Density Matrix Theory and Applications;* Plenum Press: New York, 1981.
(79) Hertel, T.; Knoesel, E.; Hotzel, A.; Wolf, M.; Ertl, G. *J. Vac. Sci. Technol., A: Vac. Surf. Films* **1997**, *15*, 1503.
(80) Wolf, M.; Hotzel, A.; Knoesel, E.; Velic, D. *Phys. Rev. B* **1999**, *59*, 5926.
(81) Ueba, H.; Mii, T. *Appl. Phys. A: Mater. Sci. Process.* **2000**, *71*, 537.
(82) Boger, K.; Roth, M.; Weinelt, M.; Fauster, T.; Reinhard, P. G. *Phys. Rev. B* **2002**, *65*, 075104.
(83) Petek, H.; Nagano, H.; Weida, M. J.; Ogawa, S. *Chem. Phys.* **2000**, *251*, 71.
(84) Boger, K.; Fauster, T.; Weinelt, M. *New J. Phys.* **2005**, *7*, 1.
(85) Boger, K.; Weinelt, M.; Wang, J.; Fauster, T. *Appl. Phys. A: Mater. Sci. Process.* **2004**, *78*, 161.
(86) Roth, M.; Pickel, M.; Weinelt, M.; Fauster, T. *Appl. Phys. A: Mater. Sci. Process.* **2004**, *78*, 149.
(87) Roth, M.; Weinelt, M.; Fauster, T.; Wahl, P.; Schneider, M. A.; Diekhoner, L.; Kern, K. *Appl. Phys. A: Mater. Sci. Process.* **2004**, *78*, 155.
(88) Schlichting, H.; Menzel, D. *Surf. Sci.* **1992**, *272*, 27.
(89) Schlichting, H.; Menzel, D. *Surf. Sci.* **1993**, *285*, 209.
(90) Merry, W. R.; Jordan, R. E.; Padowitz, D. F.; Harris, C. B. *Surf. Sci.* **1993**, *295*, 393.
(91) Rössler, U. *Phys. Status Solidi* **1970**, *42*, 345.
(92) Rössler, U. Band structure and excitons. In *Rare Gas Solids*; Academic Press: London, 1977.
(93) Narloch, B.; Menzel, D. *Chem. Phys. Lett.* **1997**, *270*, 163.
(94) Machado, M.; Berthold, W.; Höfer, U.; Chulkov, E. V.; Echenique, P. M. *Surf. Sci.* **2004**, *564*, 87.
(95) Hotzel, A.; Ishioka, K.; Knoesel, E.; Wolf, M.; Ertl, G. *Chem. Phys. Lett.* **1998**, *285*, 271.
(96) Hotzel, A.; Wolf, M.; Gauyacq, J. P. *J. Phys. Chem. B* **2000**, *104*, 8438.
(97) Knoesel, E.; Hertel, T.; Wolf, M.; Ertl, G. *Chem. Phys. Lett.* **1995**, *240*, 409.
(98) Bauer, M.; Pawlik, S.; Aeschlimann, M. *Surf. Sci.* **1997**, *377*, 350.
(99) Bauer, M.; Pawlik, S.; Aeschlimann, M. *Phys. Rev. B* **1997**, *55*, 10040.
(100) Wurth, W.; Menzel, D. *Chem. Phys.* **2000**, *251*, 141.
(101) Chiang, T. C.; Kaindl, G.; Eastman, D. E. *Solid State Commun.* **1980**, *36*, 25.
(102) Alivisatos, A. P.; Waldeck, D. H.; Harris, C. B. *J. Chem. Phys.* **1985**, *82*, 541.
(103) Höfer, U.; Breitschafter, M. J.; Umbach, E. *Phys. Rev. Lett.* **1990**, *64*, 3050.
(104) Bertolo, M.; Hansen, W.; Jacobi, K. *Phys. Rev. Lett.* **1991**, *67*, 1898.
(105) Hudel, E.; Steinacker, E.; Feulner, P. *Phys. Rev. B* **1991**, *44*, 8972.
(106) Sanche, L. *Phys. Rev. Lett.* **1995**, *75*, 3568.
(107) Sack, N. J.; Akbulut, M.; Madey, T. E. *Phys. Rev. B* **1995**, *51*, 4585.
(108) Keller, C.; Stichler, M.; Comelli, G.; Esch, F.; Lizzit, S.; Gortel, Z. W.; Wurth, W.; Menzel, D. *Phys. Rev. B* **1999**, *60*, 16143.
(109) Rohleder, M.; Duncker, K.; Berthold, W.; Gödde, J.; Höfer, U. *New J. Phys.* **2005**, *7*, 103.
(110) *CRC Handbook of Chemistry and Physics*, 74th ed.; CRC Press: Boca Raton, FL, 1994.
(111) Gödde, J.; Klinkmüller, A.; West, P. J.; Matthias, E. *Phys. Rev. A* **1993**, *47*, 4725.
(112) Berthold, W.; Höfer, U. *Isr. J. Chem.* **2005**, *45*, 181.
(113) Kliewer, J.; Berndt, R.; Chulkov, E. V.; Silkin, V. M.; Echenique, P. M.; Crampin, S. *Science* **2000**, *288*, 1399.
(114) Chulkov, E. V.; Borisov, A. G.; Gauyacq, J. P.; Sánchez-Portal, D.; Silkin, V. M.; Zhukov, V. P.; Echenique, P. M. *Chem. Rev.* **2006**, *106*, 4160−4206.
(115) Silkin, V. M.; Balasubramanian, T.; Chulkov, E. V.; Rubio, A.; Echenique, P. M. *Phys. Rev. B* **2001**, *64*, 085334.
(116) Marinica, D. C.; Ramseyer, C.; Borisov, A. G.; Teillet-Billy, D.; Gauyacq, J.; Berthold, W.; Feulner, P.; Höfer, U. *Phys. Rev. Lett.* **2002**, *89*, 046802.
(117) Marinica, D. C.; Ramseyer, C.; Borisov, A. G.; Teillet-Billy, D.; Gauyacq, J. P. *Surf. Sci.* **2003**, *528*, 78.
(118) Gödde, J.; Höfer, U. *Prog. Surf. Sci.* **2005**, *80*, 49.
(119) Giesen, K.; Hage, F.; Himpsel, F. J.; Riess, H. J.; Steinmann, W. *Phys. Rev. B* **1987**, *35*, 971.
(120) Marinica, D. C.; Ramseyer, C.; Borisov, A. G.; Teillet-Billy, D.; Gauyacq, J. P. *Surf. Sci.* **2003**, *540*, 457.
(121) Perluzzo, G.; Bader, G.; Caron, L. G.; Sanche, L. *Phys. Rev. Lett.* **1985**, *55*, 545.
(122) Zhu, X. Y. *J. Phys. Chem. B* **2004**, *108*, 8778.
(123) Szymanski, P.; Garrett-Roe, S.; Harris, C. B. *Prog. Surf. Sci.* **2005**, *78*, 1.
(124) Hertel, T.; Knoesel, E.; Hasselbrink, E.; Wolf, M.; Ertl, G. *Surf. Sci.* **1994**, *317*, L1147.
(125) Hertel, T.; Knoesel, E.; Wolf, M.; Ertl, G. *Nucl. Instrum. Methods B* **1995**, *101*, 53.
(126) Bartels, L.; Meyer, G.; Rieder, K. H.; Velic, D.; Knoesel, E.; Hotzel, A.; Wolf, M.; Ertl, G. *Phys. Rev. Lett.* **1998**, *80*, 2004.
(127) Bauer, M.; Pawlik, S.; Burgermeister, R.; Aeschlimann, M. *Surf. Sci.* **1998**, *404*, 62.
(128) Bauer, M.; Pawlik, S.; Aeschlimann, M. *Phys. Rev. B* **1999**, *60*, 5016.
(129) Ogawa, S.; Nagano, H.; Petek, H. *Phys. Rev. Lett.* **1999**, *82*, 1931.
(130) Petek, H.; Weida, L. J.; Nagano, H.; Ogawa, S. *Surf. Sci.* **2000**, *451*, 22.
(131) Petek, H.; Nagano, H.; Weida, M. J.; Ogawa, S. *J. Phys. Chem. A* **2000**, *104*, 10234.
(132) Petek, H.; Ogawa, S. *Annu. Rev. Phys. Chem.* **2002**, *53*, 507.
(133) Petek, H.; Nagano, H.; Weida, M. J.; Ogawa, S. *J. Phys. Chem. B* **2001**, *105*, 6767.
(134) Velic, D.; Hotzel, A.; Wolf, M.; Ertl, G. *J. Chem. Phys.* **1998**, *109*, 9155.
(135) Munakata, T.; Sakashita, T.; Tsukakoshi, M.; Nakamura, J. *Chem. Phys. Lett.* **1997**, *271*, 377.
(136) Munakata, T.; Shudo, K. *Surf. Sci.* **1999**, *435*, 184.
(137) Munakata, T. *J. Chem. Phys.* **1999**, *110*, 2736.
(138) Munakata, T. *Surf. Sci.* **2000**, *454*, 118.
(139) Miller, A. D.; Gaffney, K. J.; Liu, S. H.; Szymanski, P.; Garrett-Roe, S.; Wong, C. M.; Harris, C. B. *J. Phys. Chem. A* **2002**, *106*, 7636.
(140) Gaffney, K. J.; Wong, C. M.; Liu, S. H.; Miller, A. D.; McNeill, J. D.; Harris, C. B. *Chem. Phys.* **2000**, *251*, 99.
(141) Vondrak, T.; Cramer, C. J.; Zhu, X. Y. *J. Phys. Chem. B* **1999**, *103*, 8915.
(142) Vondrak, T.; Zhu, X. Y. *J. Phys. Chem. B* **1999**, *103*, 3449.
(143) Gahl, C.; Ishioka, K.; Zhong, Q.; Hotzel, A.; Wolf, M. *Faraday Discuss.* **2000**, *117*, 191.
(144) Kirchmann, P. S.; Loukakos, P. A.; Bovensiepen, U.; Wolf, M. *New J. Phys.* **2005**, *7*, 1.
(145) Lingle, R. L.; Ge, N. H.; Jordan, R. E.; McNeill, J. D.; Harris, C. B. *Chem. Phys.* **1996**, *208*, 297.
(146) Lingle, R. L.; Padowitz, D. F.; Jordan, R. E.; McNeill, J. D.; Harris, C. B. *Phys. Rev. Lett.* **1994**, *72*, 2243.
(147) Höfer, U. *Science* **1998**, *279*, 190.
(148) Bezel, I.; Gaffney, K. J.; Garrett-Roe, S.; Liu, S. H.; Miller, A. D.; Szymanski, P.; Harris, C. B. *J. Chem. Phys.* **2004**, *120*, 845.
(149) Liu, S. H.; Miller, A. D.; Gaffney, K. J.; Szymanski, P.; Garrett-Roe, S.; Bezel, I.; Harris, C. B. *J. Phys. Chem. B* **2002**, *106*, 12908.

(150) Gahl, C.; Bovensiepen, U.; Frischkorn, C.; Morgenstern, K.; Rieder, K. H.; Wolf, M. *Surf. Sci.* **2003**, *532*, 108.
(151) Bovensiepen, U.; Gahl, C.; Wolf, M. *J. Phys. Chem. B* **2003**, *107*, 8706.
(152) Bovensiepen, U.; Gahl, C.; Stähler, J.; Loukakos, P. A.; Wolf, M. *Isr. J. Chem.* **2005**, *45*, 171.
(153) Andrianov, I.; Klamroth, T.; Saalfrank, P.; Bovensiepen, U.; Gahl, C.; Wolf, M. *J. Chem. Phys.* **2005**, *122*, 234710.
(154) Bovensiepen, U. *Prog. Surf. Sci.* **2005**, *78*, 87.
(155) Dutton, G.; Zhu, X. Y. *J. Phys. Chem. B* **2002**, *106*, 5975.
(156) Dutton, G.; Pu, J.; Truhlar, D. G.; Zhu, X. Y. *J. Chem. Phys.* **2003**, *118*, 4337.
(157) Chulkov, E. V.; Silkin, V. M.; Echenique, P. M. *Surf. Sci.* **1997**, *391*, L1217.

CR050171S